



Norwegian University of
Science and Technology

Estimation of Thermal Properties of an Ice Pad using the Parameter Particle Filter

Fredrik Elis Lundquist

Master of Science in Physics and Mathematics

Submission date: July 2017

Supervisor: Karl Henning Omre, IMF

Norwegian University of Science and Technology
Department of Mathematical Sciences

Preface

This study was carried out in the Department of Mathematical Sciences at the Norwegian University of Science and Technology, Trondheim, Norway, during the spring of 2017. The study marks the completion of the five-year Industrial Mathematics program at NTNU and leads to the Master of Science degree.

At the beginning of this project, I, along with a team from Senter for idrettsanlegg og teknologi (SIAT), went to Hamar Olympic Hall to install temperature sensors. There were many complications during the installation process, forcing us to abandon the project at Vikingskipet. Instead, Schjonghallen, Hønefoss, was used as experimental basis for this study.

Much time was spent developing the heat transfer model in COMSOL, and with the help of Christian Schlemminger at SINTEF Building and Infrastructure, we managed to implement it. With the heat transfer successfully in place, I undertook the implementation of the Parameter Particle Filter we used. I faced no major problems thanks to the help of Jacob Skauvold, IMF/NTNU.

I wish to thank my supervisor, Henning Omre, for all his support. I also want to thank the people at SIAT for providing helpful insights and a wonderful working environment. Lastly, I would like to thank my mother, and my girlfriend, Kristine, for all their support.

Abstract

Heating is the primary energy consumer in an ice rink, and the ability to optimise its use is a key factor in minimising energy expenditures. This study performs parameter estimation on site-specific thermal parameters using a Particle Filter. A numerical scheme of the transient heat conduction is developed, and the temperature distribution is simulated using COMSOL. The thermal conductivity of an ice rink floor is estimated using synthetic data, and the results show that this version of the Particle Filter is able to successfully estimate the target parameter.

Sammendrag

Energiforbruket i ishaller går hovedsakelig til oppvarming. Det er derfor viktig å effektivisere bruken av energi som går til oppvarming. Denne oppgaven tar for seg parameterestimasjon av stedsavhengige termiske parametere ved bruk av et partikkelfilter. Et numerisk skjema for varmeledningen utvikles og temperaturfordelingen blir simulert ved bruk av COMSOL. Varmeoverføringskoeffisienten i en ishall blir så estimert ved bruk av syntetiske data. Resultatene indikerer at versjonen av partikkelfilteret utviklet i denne oppgaven lykkes i å estimere den undersøkte parameteren.

Contents

1	Introduction	1
1.1	Notation and Assumptions	4
2	Heat Flow Model	7
2.1	Transient Heat Conduction	9
2.2	Simulations of the Transient Heat Conduction	13
3	Statistical Model	17
3.1	Model Assumptions and Framework	17
3.2	Prior Model	18
3.3	Likelihood Model	20
3.4	Posterior Model	21
3.5	Traditional Kalman Filter	22
3.6	Ensemble Kalman Filter	25
3.7	Particle Filter	27
3.8	Parameter Particle Filter	28
4	Case Study	33
4.1	Synthetic Data	34
4.2	Weight Distribution	37
4.3	Empirical Model Parameter Distribution	44
4.4	Discussion of the Test Case	47
5	Closing Remarks	51
	Bibliography	53

Chapter 1

Introduction

Most of the published research on ice rinks focus on energy savings by optimising the performance of the major components, such as heating, cooling and ventilation (Mun & Krarti, 2015; Gonzalez, 2002; Ferrantelli & Viljanen, 2015). Because 43% of the energy used in an ice rink originates from the cooling system, understanding and optimising this component is vital to achieving an energy efficiency (Rogstam & Hjert, 2010). This study focuses on the temperature distribution within the floor of an ice rink and develops a method of estimating the site-specific thermal parameters using the Parameter Particle Filter.

Ice pads differ from traditional building foundations because they contain a piping system, a refrigeration unit and a heating component. Thus, analysing the characteristics of an ice pad cannot be performed using the same methods established for regular building foundations. Somrani et al. (2008) investigate the heat transfer beneath the ice pad using a finite difference scheme and an analytical solution. They are particularly interested in the temperature change in the soil beneath the ice pad. Their numerical method accounts for details such as pipe composition and di-

mension, size and volume of the water/ice layer and the insulation layer beneath the pipes. Assuming that heat flux to the soil surface is governed by Newton's law, they develop an implicit numerical scheme with converging results.

The authors conduct a laboratory test using plywood sheets, copper and plastic pipes and foam boards to verify the results. Using this approach, they analyse the impact of certain parameters: floor insulation, water/ice thickness, brine temperature, indoor temperature and convective heat transfer above the ice pad. The study's main finding is that the use of floor insulation reduced the freezing time by more than 40%. Moreover, a thicker water/ice layer increased freezing time, as did higher indoor temperature and higher convective heat transfer above the ice pad. Maintaining the cooling brine at a lower temperature, reduced freezing time.

Ferrantelli and Viljanen (2015) examine temperature development in and the heat flux on the ice pad in an ice rink in Finland. They measure the temperature and heat flux during both the cooling of the ice and when the water had frozen. The main contributors to heat flux on the slab is ceiling radiation (74%), lighting (14%), convection from water vapour (10%) and condensation (2%). The authors also develop a generic formula for calculating the temperature in the ice pad given proper boundary conditions. The boundary conditions used in the study is derived from measurements made in the ice rink.

Mun and Krarti (2011) propose a heat transfer model with the intent of integrating it into whole-building simulations for an ice rink. They model the ice rink floor using the conduction transfer function method and integrates the process into a general building simulation using EnergyPlus, a simulation program for buildings. The study's main focus is the simulation and verification of the effect on the ice pad's temperature and heat flux

by considering the two most commonly used control methods: brine outlet temperature and ice surface temperature. Using a small scale model, the simulations are verified during laboratory conditions. The results show that even though controlling the temperature in the ice slab by monitoring the temperature of the cooling brine uses slightly less energy, the ability to achieve constant temperature in the ice slab by basing the temperature controls on the ice surface temperature is preferred.

Mun and Krarti (2015) also analyses the optimal insulation for an ice pad with regard to the pad's location and composition. Expanding on their previously proposed model, they add a life cycle cost function, which considers the cost of energy use, installation and material in order to determine the optimal insulation material and thickness. This model is tested in three US locations with different climates; cold (Anchorage, Alaska), mild (Boulder, Colorado) and warm (Tampa Bay, Florida). They find that in all three locations, an insulation layer reduced the refrigeration cost. Moreover, they find a linear relation between the mean ground temperature and the thickness of the isolation.

In this report, we define a special version of the Particle Filter, called the Parameter Particle Filter in order to estimate the time-constant thermal conductivity of the ice rink. The forward model can be run only once, making the Ensemble Kalman Filter and the traditional Particle Filter difficult to use. To update the state space, the temperature profiles of the low-weighted particles are shifted near the profiles of the high-weighted particles. Finally, a parameter update is performed using an estimated Ensemble Kalman update. In this report, only the thermal conductivity is estimated; the density and specific heat capacity are assumed to be known and constant.

1.1 Notation and Assumptions

The following notation is used throughout this study. The bold letter, \mathbf{x} , is used to denote a spatial vector, and matrices are denoted by bold capital letter \mathbf{A} . Random variables \mathbf{v} with probability density function (PDF) $f(\mathbf{v})$ are denoted by $\mathbf{v} \sim f(\mathbf{v})$. In this study, $\phi_n(\mathbf{v}; \boldsymbol{\mu}_v, \boldsymbol{\Sigma}_v)$, is the multivariate normal distribution

$$\mathbf{v} \sim \phi_n(\mathbf{v}; \boldsymbol{\mu}_v, \boldsymbol{\Sigma}_v) = [2\pi]^{-n/2} |\boldsymbol{\Sigma}_v|^{-1/2} \exp \left\{ -\frac{1}{2} (\mathbf{v} - \boldsymbol{\mu}_v)^T \boldsymbol{\Sigma}_v^{-1} (\mathbf{v} - \boldsymbol{\mu}_v) \right\},$$

where $\boldsymbol{\mu}_v$ and $\boldsymbol{\Sigma}_v$ are the expectation and covariance, respectively. Several assumptions are made to facilitate calculations and due to the lack of information in certain areas. First, the simulated model in this study is two-dimensional. Therefore, the sensors have to be placed at an equal distance from the boards such that they all align with respect to a cross section. The boundary conditions are considered constant in the simulations, because the sensors are placed far enough from the boards, such that this is a reasonable assumption. However, if the sensors are at different distances from the boards, the boundary conditions may not be constant. The setup of the cooling pipes is shown in Figure 1.1.

Next, in the simulations for calculating the temperature at different time steps, two assumptions are made. The first is that the gravel and dirt layer beneath the insulation layer is not modelled. Compared to the other layers, the depth of this layer is practically indefinite, rendering it unnecessary to model. It is instead considered a boundary condition. The boundary condition is modelled such that the heat flux from the heating pipes is considered uniform and constant, giving a constant temperature at the



Figure 1.1: Cooling pipes in the concrete. The pipes cover the whole rink and alternate between inbound and outbound. Although the picture is from Hamar Olympic Hall, the same setup is used in Schjong Ice Rink.

lower boundary of the insulation layer. The reference values for the heat flux and temperature are derived from data given by a sensor placed below the insulation layer and from data given by Ringerike Municipality.

The second assumption with regarding the simulation is that the cooling pipes in the concrete are modelled simply as circles with a constant temperature and can be considered heat sinks. In actuality, these pipes have metallic or plastic outer walls and a cooling brine within. Both the walls of the pipe and the cooling brine have different thermal properties, leading to a more complicated expression for the heat flux from the pipes.

This report is organised as follows. In Chapter 2, the transient heat equation is derived and a numerical scheme for approximating it is suggested. Chapter 3 presents the common approaches to solving problems in a Bayesian framework, such as the Kalman Filter and Particle Filter, and also develops a Particle Filter with parameter estimation, which will later

CHAPTER 1. INTRODUCTION

be used to estimate site-specific thermal parameters. Chapter 4 tests the Particle Filter developed Chapter 3 on a test case using synthetic data. In Chapter 5, we present some closing remarks and suggest avenues for future research.

Chapter 2

Heat Flow Model

Ice rinks use cooling liquid inside pipes to regulate the temperature of the ice pad. A typical ice pad is constructed from two layers of concrete or gravel and a layer of insulation (Gonzalez, 2002), as shown in Figure 2.1. The cooling brine transported in the pipes is usually some form of glycogen, but it varies from country to country and is subject to rules and regulations.

This study examines the ice pad in Schjonghallen, in Hønefoss, and all assumptions in the following heat model are based on the schematics of this ice pad. A two-dimensional system is proposed with $\mathbf{x} = (x_a, x_b)$ as the spatial variable. Let the time be $\mathbf{T} = [0, 1, 2, \dots, t - 1, t, t + 1, \dots, T]$, where t is the current time and $t + 1$ is the predicted time. The details of the ice pad used in this study are given in Figure 2.2.

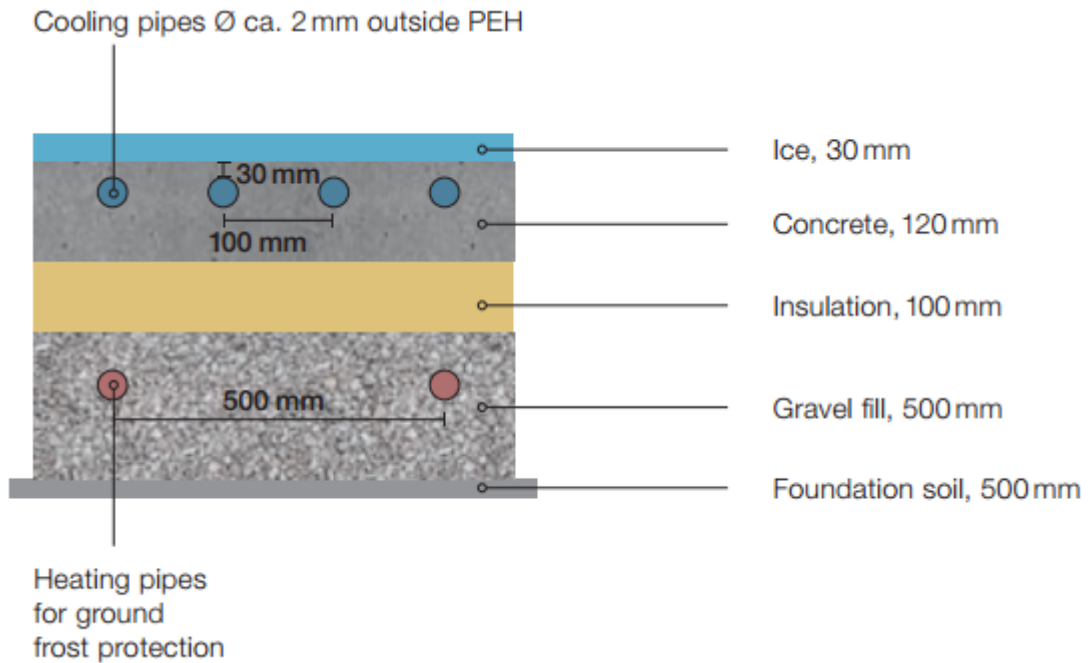


Figure 2.1: Typical ice-pad structure. Image from the International Ice Hockey Federation's technical handbook.

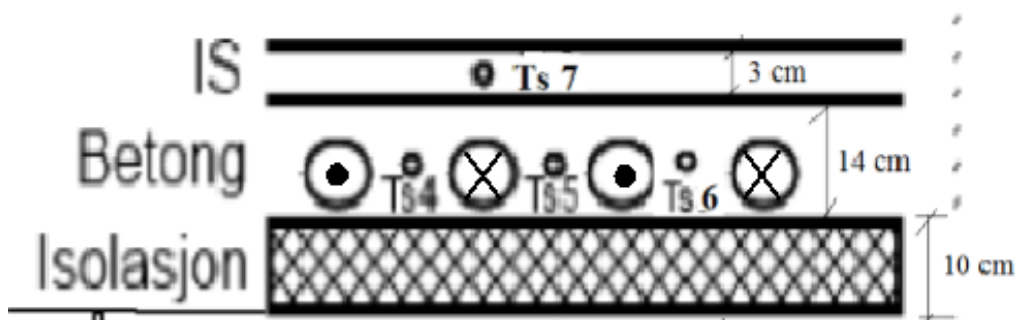


Figure 2.2: Ice pad, Sjong Ice Rink. Top layer is ice, middle layer is concrete and bottom layer is insulation.

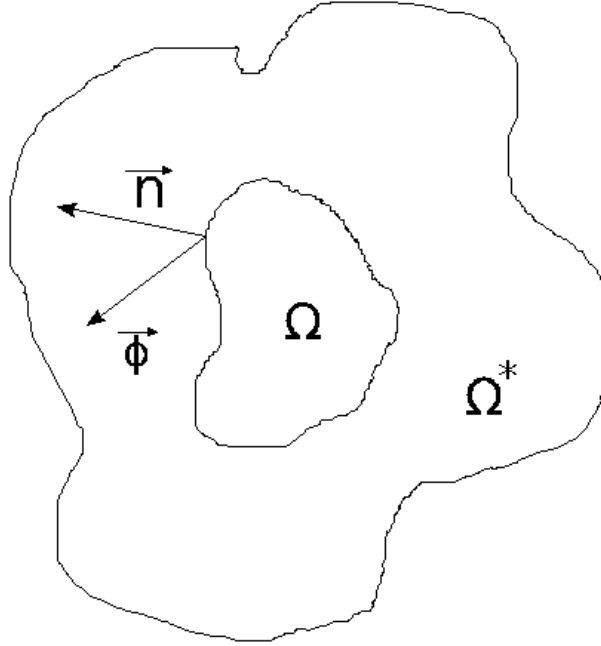
2.1 Transient Heat Conduction

This study develops a numerical scheme for the transient heat conduction from cooling pipes through the layers of ice, concrete and insulation. Generally, heat flow is modelled by the heat equation, which can be derived the heat flux of a volume element, $\Omega \subset \Omega^*$ (see Figure 2.3). For an extensive derivation of the nonstationary heat equation, see, for example, (Zieniuk, Sawicki, & Boltuc, 2014; DeWitt & Baliga, 1982; Widder, 1976) and references therein. We consider only two dimensions, such that the volume element, Ω , reduces to a plane segment fully described by the space variable \mathbf{x} . Let $Q(\mathbf{x}, t)$ be the internal heat source of the plane segment and $S(\mathbf{x}) = \partial\Omega$ be the border of Ω . Then, at a given time t , the internal heat can be fully described by the heat flux leaving the plane segment across the entirety of its border, $\partial\Omega$, that is,

$$\iint_{\mathbf{x} \in \Omega} Q(\mathbf{x}, t) d\mathbf{x} = \int_S \vec{\phi}(S(\mathbf{x}), t) \cdot \vec{n}(S(\mathbf{x})) d\mathbf{x}, \quad (2.1)$$

where $\vec{\phi}(\mathbf{x}, t)$ is the heat flux leaving the plane segment and $\vec{n}(S(\mathbf{x}))$ is the unit normal vector perpendicular to Ω as shown in Figure 2.3. The left-hand side of Equation (2.1) is the volume integral, and the right hand side is the surface integral.

The divergence theorem provides a relation between the outgoing flux of a vector field and the internal behaviour of the field. In other words, the outgoing flux through the surface is equal to the volume integral of the divergence of the vector field (Pfeffer, 1986). The outgoing flux is the heat flux, $\vec{\phi}(\mathbf{x}, t)$, through the surface $S(\mathbf{x})$, and the surface integral in Equation (2.1) can be expressed as


 Figure 2.3: Heat flow from Ω .

$$\int_S \vec{\phi}(\mathbf{x}, t) \cdot \vec{n}(S(\mathbf{x})) d\mathbf{x} = \iint_{\mathbf{x} \in \Omega} \nabla_{\mathbf{x}} \vec{\phi}(\mathbf{x}, t) d\mathbf{x}, \quad (2.2)$$

with both the internal heat, $Q(\mathbf{x}, t)$, and the heat flux, $\vec{\phi}(\mathbf{x}, t)$, expressed as volume integral over Ω . Then, Equation (2.1) simplifies into

$$\iint_{\mathbf{x} \in \Omega} \left(Q(\mathbf{x}, t) - \nabla_{\mathbf{x}} \vec{\phi}(\mathbf{x}, t) \right) d\mathbf{x} = 0, \quad (2.3)$$

$\forall t$. The observable variable is the temperature, $U(\mathbf{x}, t)$, which is both spatially and temporally dependent. Using the differential form of Fourier's law, which states that the heat through a volume element is proportional to the negative gradient of the temperature (Han, Nie, Chen, & Wang, 2015)

$$\vec{\phi}(\mathbf{x}, t) = -\lambda(\mathbf{x}) \nabla_{\mathbf{x}} U(\mathbf{x}, t), \quad (2.4)$$

where $\lambda(\mathbf{x})$ is the thermal conductivity (DeWitt & Baliga, 1982), Equation (2.3) can be written as

$$Q(\mathbf{x}, t) + \nabla_{\mathbf{x}}^2(\lambda(\mathbf{x})U(\mathbf{x}, t)) = 0, \quad (2.5)$$

$\forall t = 0, \dots, T$, which is the steady-state, that is, the time independent heat equation. When considering temporal dependency, the transient heat equation is found by applying the first principle of thermodynamics, which states that the heat brought on the volume element results in an internal energy change on the domain over time (Bergheau, 2010). This change over time in the enthalpy can be expressed as

$$\rho(\mathbf{x})\frac{\partial H(t)}{\partial t} = \rho(\mathbf{x})c_p(\mathbf{x})\frac{\partial U(\mathbf{x}, t)}{\partial t}, \quad (2.6)$$

where $\rho(\mathbf{x})$ is the density of the plane segment and $c_p(\mathbf{x})$ is the specific heat capacity. Then, Equation (2.5) becomes

$$Q(\mathbf{x}, t) + \lambda(\mathbf{x})\nabla_{\mathbf{x}}^2U(\mathbf{x}, t) = \rho(\mathbf{x})c_p(\mathbf{x})\frac{\partial U(\mathbf{x}, t)}{\partial t}. \quad (2.7)$$

Now we discretise $\mathbf{x} = [x_0, x_1, \dots, x_T]$ in order to numerically approximate Equation (2.7). Let $U_{m,n}^t = U(\mathbf{x}^*, t)$, as shown in Figure 2.4, where $\mathbf{x}^* = (m, n)$, and consider a first-order differencing in time and second-order differencing in space. Then, we have

$$\frac{\partial U(\mathbf{x}^*, t)}{\partial t} = \frac{U_{m,n}^{t+1} - U_{m,n}^t}{\Delta t} \quad (2.8)$$

$$\frac{\partial^2 U(\mathbf{x}^*, t)}{\partial(\mathbf{x})^2} = \frac{U_{m+1,n}^t - 2U_{m,n}^t + U_{m-1,n}^t}{\Delta x_a^2} + \frac{U_{m,n+1}^t - 2U_{m,n}^t + U_{m,n-1}^t}{\Delta x_b^2}, \quad (2.9)$$

with $\Delta x_a, \Delta x_b, \Delta t$ being the increments in x_a, x_b and t direction, respectively. With this notation, the transient heat conduction in Equation (2.7) can be expressed as

$$\begin{aligned} Q(\mathbf{x}^*, t) + \lambda(\mathbf{x}^*) \left[\frac{U_{m+1,n}^t - 2U_{m,n}^t + U_{m-1,n}^t}{\Delta x_a^2} + \frac{U_{m,n+1}^t - 2U_{m,n}^t + U_{m,n-1}^t}{\Delta x_b^2} \right] \\ = \rho(\mathbf{x}^*) c_p(\mathbf{x}^*) \left[\frac{U_{m,n}^{t+1} - U_{m,n}^t}{\Delta t} \right]. \end{aligned} \quad (2.10)$$

For future referencing, let Equation (2.10) be denoted by

$$\mathbf{u}_{t+1} = \omega(\mathbf{u}_t, \lambda(\mathbf{x}^*), \rho(\mathbf{x}^*), c_p(\mathbf{x}^*)). \quad (2.11)$$

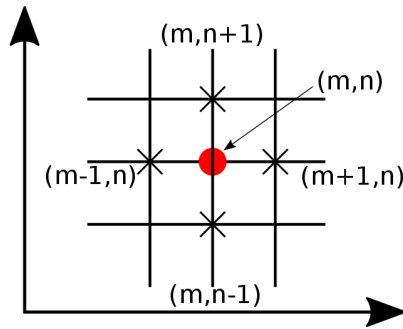


Figure 2.4: Grid system for U_t .

2.2 Simulations of the Transient Heat Conduction

Table 2.1 gives an overview of the parameter values used in the simulation. These values are given by the Property Administration in Ringerike municipality, where the Schjong Ice Rink is located. The site-specific energy related parameters $\lambda(\mathbf{x})$, $\rho(\mathbf{x})$, $\mathbf{c}_p(\mathbf{x})$ are all spatially piecewise constant dependent on the material.

Table 2.1: Properties of the materials for the reference simulation.

	$U(\mathbf{x}, 0)$ [$^{\circ}C$]	$\mathbf{c}_p(\mathbf{x})$ [$\frac{kgm^2}{gKs^2}$]	Width [m]	$\rho(\mathbf{x})$ [$\frac{kg}{m^3}$]	$\lambda(\mathbf{x})$ [$\frac{W}{mK}$]
Outbound pipe	-8	—	0.05	—	—
Inbound pipe	-6	—	0.05	—	—
Ice slab	-2	2.03	0.035	917.5	2.24
Concrete	0	0.75	0.14	2300.0	1.00
Insulation	5	1131	0.1	5×10^{-8}	0.003

The transient heat conduction expressed by Equation (2.7) can be solved analytically by complex variable techniques and the ITPE method developed in (Somrani et al., 2008), but we apply the simulation program COMSOL. This program allows us create a geometry with individual domains that can be specified to mimic the properties of different materials. It also lets us define heat sources, and can, amongst many other capabilities, monitor the temperature distribution throughout the geometry at any given time t . Figure 2.5 shows the temperature distribution throughout the simulated ice pad initially, that is, at $t = 0$.

The white circles in Figure 2.5 represent the cooling pipes, which are held at constant temperature during simulations. The middle pipe is the inbound pipe and is held at $T_{in} = -6^{\circ}C$, and the left and right pipes are

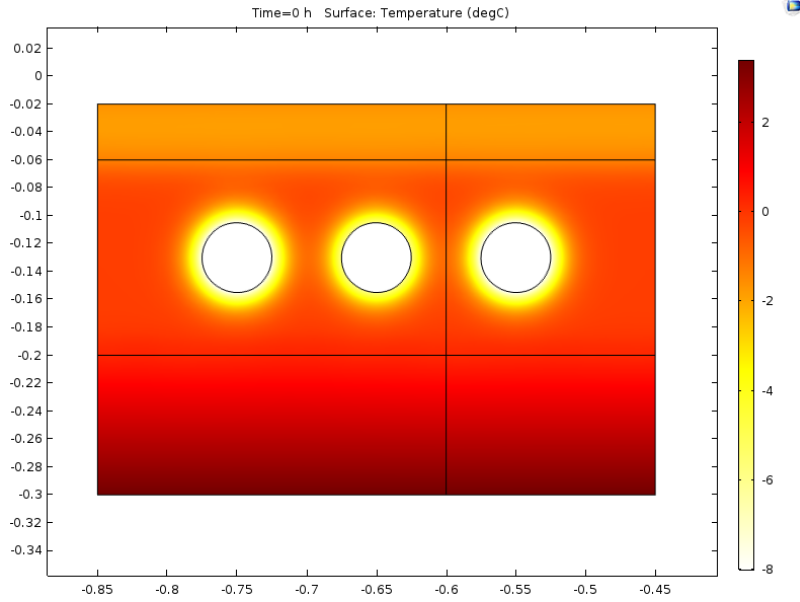


Figure 2.5: Simulations of the temperature using COMSOL, at $t = 0$. Top layer is the ice slab, middle layer is the concrete containing the cooling pipes (from left: outbound, inbound, outbound) and bottom layer the insulation layer.

outbound and held at at $T_{out} = -8^{\circ}C$. The top layer is the ice slab, and the middle layer, which contains the cooling pipes, is concrete. The bottom layer is the insulation layer, and below that is the layer of dirt and soil which contains heating pipes to prevent freezing. The dirt-and-soil layer is not included in the simulations, because the dimension is practically unbounded with in comparison to the other layers. At the end of the simulation, $t = 24$, we have reached a steady-state solution, as shown in Figure 2.6.

Figure 2.6 shows that both the concrete and ice layers reach a steady state solution around $-3^{\circ}C$, whereas the insulation layer varies in temperature depending on the distance from the cooling pipes. A cross section of the temperature distribution at $t = 0$ is plotted in Figure 2.7.

The cross section is set up such that the x-axis starts at the bottom of the vertical line and follows it to the end, which represents the ice surface. Figure 2.8 shows the temperature distribution at $t = 24$.

2.2. SIMULATIONS OF THE TRANSIENT HEAT CONDUCTION

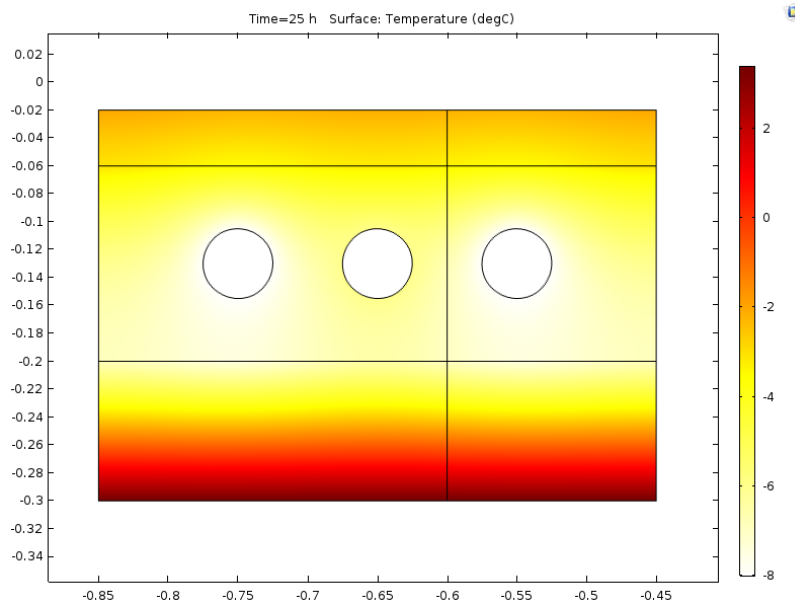


Figure 2.6: Surface temperature distribution at $t = 24$.

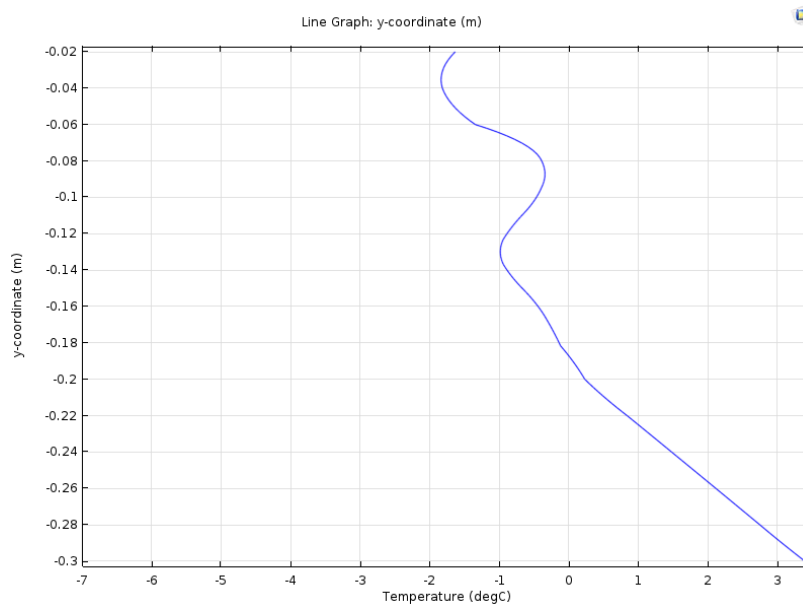


Figure 2.7: Cross section of the temperature distribution at $t = 0$.

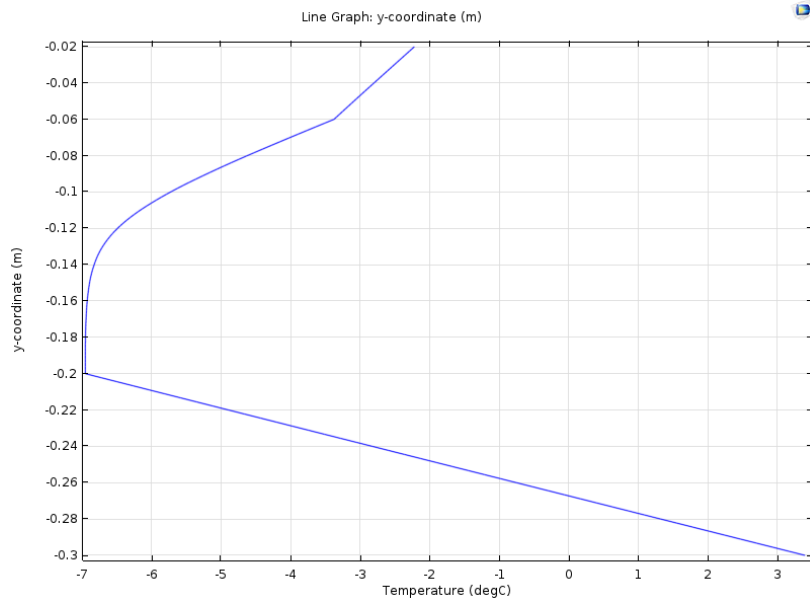


Figure 2.8: Cross section of the temperature distribution at $t = 24$.

Here, the temperature drops off linearly as we go through the insulation and reach the cooling pipes. The temperature then stabilises at around -2°C as it reaches the ice and the heat flux from the air in the ice rink becomes significant.

Chapter 3

Statistical Model

For state space estimation problems such as the one in this study, Bayesian methods are commonly used. The idea is to create a PDF of the state, given all previously available information (Gordon et al., 1993).

If the problem in question is Gaussian-linear, the problem will remain Gaussian at every iteration over \mathbf{x} and an analytical solution can be found. However, when considering nonlinear non-Gaussian systems, a general analytical solution is not readily available, because the normalising constant is usually hard to assess.

3.1 Model Assumptions and Framework

The basis of our consideration is the spatial-temporal random variable of the temperature in the ice pad, $u(\mathbf{x}, t)$, which is the temperature at location \mathbf{x} and at time $t = [0, \dots, T]$. For convenience, let $u(\mathbf{x}, t)$ be expressed as

$$\begin{aligned}\mathbf{u}(\mathbf{x}) &= [u(\mathbf{x}, 0), \dots, u(\mathbf{x}, T)] \\ &= [\mathbf{u}_0, \dots, \mathbf{u}_T]; \mathbf{x} \in \mathbb{R}^{n_x}.\end{aligned}$$

Then, the temperature, $\mathbf{u}(\mathbf{x})$, is a p_u -dimensional random variable. Moreover, the heat source $q(\mathbf{x}, t)$ is considered constant throughout the study. The heat source consists of two cooling pipes that transports cooling brine to and from the ice rink. Their temperature is held constant throughout the study, and the temperature in the outbound pipe is lower than that in the inbound pipe. The initial state of $\mathbf{u}(\mathbf{x})$, $u(\mathbf{x}, 0)$, is given as initial conditions as presented in Figure 2.7. These initial conditions are considered the prior model with regards to Bayesian inference.

3.2 Prior Model

Let the model parameters $\lambda(\mathbf{x})$, $\rho(\mathbf{x})$ and $c_p(\mathbf{x})$ be temporally constant and spatially piecewise constant and be assigned independent Gaussian PDFs

$$[\lambda|\kappa] \sim f(\lambda|\kappa) = \phi_1(\lambda; \mu_{\lambda|\kappa}, \sigma_{\lambda|\kappa}^2)$$

$$[\rho|\kappa] - \text{known}$$

$$[c_p|\kappa] - \text{known}$$

where $\kappa \in \{\text{ice, concrete, insulation}\}$. This study focuses on $\lambda|\kappa$, and in order to simplify the model, $\rho|\kappa$ and $c_p|\kappa$ are considered known. The random variable of interest is then

$$\mathbf{v}_t = \begin{bmatrix} \mathbf{u}_t \\ \boldsymbol{\lambda} \end{bmatrix}.$$

with initial state

$$\mathbf{v}_0 = \begin{bmatrix} \mathbf{u}_0 \\ \boldsymbol{\lambda} \end{bmatrix} \sim f(\mathbf{v}_0)$$

defined by the prior model discussed above. The following recursion is defined by the heat relations in Equation (2.11):

$$[\mathbf{v}_t | \mathbf{v}_{t-1}] = \begin{bmatrix} \mathbf{u}_t \\ \boldsymbol{\lambda} \end{bmatrix} = \begin{bmatrix} \omega(\mathbf{u}_{t-1}; \boldsymbol{\lambda}) \\ \boldsymbol{\lambda} \end{bmatrix},$$

which is a deterministic relation represented by $f(\mathbf{v}_t | \mathbf{v}_{t-1})$, being a Dirac PDF. The joint probability is then

$$[\mathbf{v}_0, \dots, \mathbf{v}_T] \sim f(\mathbf{v}_0, \dots, \mathbf{v}_T) \tag{3.1}$$

$$= f(\mathbf{v}_0) \prod_{t=0}^T f(\mathbf{v}_t | \mathbf{v}_0, \dots, \mathbf{v}_{t-1}) \tag{3.2}$$

$$= f(\mathbf{v}_0) \prod_{t=0}^T f(\mathbf{v}_t | \mathbf{v}_{t-1}), \tag{3.3}$$

where on the last line of the equation comes from the Markov properties, $f(\mathbf{v}_t | \mathbf{v}_0, \dots, \mathbf{v}_{t-1}) = f(\mathbf{v}_t | \mathbf{v}_{t-1})$, assumed for the heat flow model in Sec-

tion 5. This study focuses on the time-constant site-specific energy-related parameter $\lambda|\kappa$, where $\kappa \in \{\text{ice, concrete, insulation}\}$. The parameters $\rho|\kappa$ and $c_p|\kappa$, are, as previously noted, assumed to be known and constant throughout the study and will not be subject to estimation.

3.3 Likelihood Model

Let $\mathcal{L}_o \rightarrow \mathbf{x}^o = (x_1^o, \dots, x_4^o)$ be the four grid points closest to the corresponding locations of the sensor. The observations are connected to the different states through likelihood functions, $f(\mathbf{o}_t|\mathbf{v}_t)$, $t = 0, \dots, T$. These likelihoods are given by assuming conditional independence and single-site dependence, meaning the observations are conditionally independent of each other and dependent only on their corresponding state, that is,

$$\begin{aligned}
 [\mathbf{o}_0, \dots, \mathbf{o}_T | \mathbf{v}_0, \dots, \mathbf{v}_T] &\sim f(\mathbf{o}_0, \dots, \mathbf{o}_T | \mathbf{v}_0, \dots, \mathbf{v}_T) \\
 &= \prod_{t=0}^T f(\mathbf{o}_t | \mathbf{v}_0, \dots, \mathbf{v}_T) \\
 &= \prod_{t=0}^T f(\mathbf{o}_t | \mathbf{v}_t), \tag{3.4}
 \end{aligned}$$

with

$$[\mathbf{o}_t | \mathbf{v}_t] = \mathbf{H}\mathbf{v}_t + \boldsymbol{\epsilon}_t \sim f(\mathbf{o}_t | \mathbf{v}_t) = \phi_4(\mathbf{o}_t; \mathbf{u}_t^o, \sigma_\epsilon^2 \mathbf{I}_4),$$

where $\boldsymbol{\epsilon}_t \sim \phi_4(\boldsymbol{\epsilon}; \mathbf{0}, \sigma_\epsilon^2 \mathbf{I}_4)$, \mathbf{H} is a selection matrix and \mathbf{u}_t^o is the temperature distribution in the four observable grid points. The corresponding hidden

Markov model is shown in Figure 3.1. The transition from one state to another, denoted by the horizontal arrow, is governed by the transient heat conduction, that is, Equation (2.11). The likelihood in Equation (3.4) indicates that the observation at time t is dependent only on the state \mathbf{v}_t and independent of previous observation. For this study, the likelihood model is Gaussian-linear.

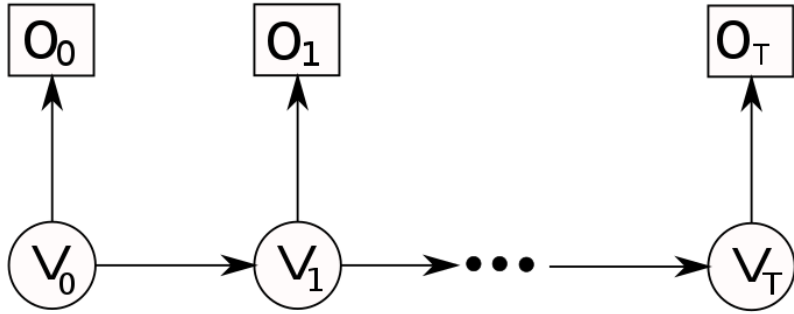


Figure 3.1: The Markov properties of the system.

3.4 Posterior Model

With the prior, $f(\mathbf{v}_0, \dots, \mathbf{v}_T)$, and the likelihood function, $f(\mathbf{o}_0, \dots, \mathbf{o}_T | \mathbf{v}_0, \dots, \mathbf{v}_T)$, known, inferences about the posterior, $[\mathbf{v}_0, \dots, \mathbf{v}_T | \mathbf{o}_0, \dots, \mathbf{o}_T]$, can be made through Bayesian inversion:

$$[\mathbf{v}_0, \dots, \mathbf{v}_T | \mathbf{o}_0, \dots, \mathbf{o}_T] \sim f(\mathbf{v}_0, \dots, \mathbf{v}_T | \mathbf{o}_0, \dots, \mathbf{o}_T) \quad (3.5)$$

$$= \text{const} \times f(\mathbf{o}_0, \dots, \mathbf{o}_T | \mathbf{v}_0, \dots, \mathbf{v}_T) \times f(\mathbf{v}_0, \dots, \mathbf{v}_T) \quad (3.6)$$

$$= \text{const} \times f(\mathbf{o}_0 | \mathbf{v}_0) f(\mathbf{v}_0) \prod_{t=1}^T f(\mathbf{o}_t | \mathbf{v}_t) f(\mathbf{v}_t), \quad (3.7)$$

where the constant is usually difficult to assess analytically. The forecast $[\mathbf{v}_T | \mathbf{o}_0, \dots, \mathbf{o}_T]$ seeks prediction regarding a single state at time T and can be assessed by integrating out $\mathbf{v}_0, \dots, \mathbf{v}_{T-1}$ from the posterior in Equation (3.5):

$$[\mathbf{v}_T | \mathbf{o}_0, \dots, \mathbf{o}_T] \sim f(\mathbf{v}_T | \mathbf{o}_0, \dots, \mathbf{o}_T) = \int \cdots \int f(\mathbf{v}_0, \dots, \mathbf{v}_T | \mathbf{o}_0, \dots, \mathbf{o}_T) d\mathbf{v}_0 \cdots d\mathbf{v}_{t-1}.$$

A common approach to solving nonlinear Bayesian prediction/estimation problems is the use of recursive numerical approximations, more commonly known as Monte Carlo methods.

3.5 Traditional Kalman Filter

In a celebrated paper, Kalman (1960), consider communication problems, especially prediction of random signals, separation of random signals from random noise and detection of random signals from random noise. He solves the Wiener-Hopf integral equation using conditional distributions and expectations. His central idea is that the observed signal is a composition of the desired signal and random noise, the desired signal can be found by considering it a conditional distribution on the previous observations. The main topic of Kalman's paper is the solution of the Wiener problem, and the theorem he gives for solving it is adapted as the Kalman Filter (Kalman, 1960). The theorem gives the optimal estimate of the desired signal and states the recursive formulae for the covariance and transitions matrices. This filter computes the posterior by recursively updating finite dimensional statistics when the system is linearised and the noise is Gaussian (Gustafsson, 2010). This extension to the Kalman Filter is known as

the Extended Kalman Filter (EKF). There may be inconsistencies when the system is mildly nonlinear and multimodal.

Several other methods stem from the Kalman Filter and EKF (Gustafsson, 2010). The unscented Kalman Filter takes a number of points in the state space and propagates them, from which a Gaussian distribution is fitted. This filter is generally more accurate than the EKF (Julier et al., 1995). Another filter is the Gaussian sum filter, which can handle multimodality by representing the posterior as Gaussian mixture distributions (Alspach & Sorenson, 1972). When the dimensionality is low, the Point Mass Filter can be applied to any nonlinear non-Gaussian model. This filter grids the entire state space and recursively computes the posterior. Because the filter is quadratic in complexity, the computing cost and time increases significantly as the dimensions increases (Kramer & Sorenson, 1988).

A key assumption of the Traditional Kalman Filter, is that the forward model is Gauss-linear and that the likelihood is linear with Gaussian noise term. Assuming that that the nonlinear $\omega(\mathbf{u}_t; \boldsymbol{\lambda})$ can be linearised such that

$$[\mathbf{v}_{t+1}|\mathbf{v}_t] = \mathbf{W}\mathbf{v}_t + \boldsymbol{\epsilon}_t^v, \quad (3.8)$$

where $\boldsymbol{\epsilon}_t^v \sim \phi_{p_u}(\boldsymbol{\epsilon}; \mathbf{0}, \sigma_v^2 \mathbf{I}_{p_u})$, then the associated Gauss-linear model is

$$\begin{aligned} \mathbf{v}_0 &\sim f(\mathbf{v}_0) = \phi_{p_u}(\mathbf{v}; \boldsymbol{\mu}_0^v, \boldsymbol{\Sigma}_0^v) \\ [\mathbf{v}_{t+1}|\mathbf{v}_t = v_t] &= \mathbf{W}\mathbf{v}_t + \boldsymbol{\epsilon}_t^v \sim f(\mathbf{v}_{t+1}|\mathbf{v}_t) = \phi_{p_u}(\mathbf{v}; \mathbf{W}\mathbf{v}_t, \boldsymbol{\Sigma}_t^v) \\ [\mathbf{o}_t|\mathbf{v}_t = v_t] &= \mathbf{H}_t\mathbf{v}_t + \boldsymbol{\epsilon}_t^o \sim f(\mathbf{o}_t|\mathbf{v}_t) = \phi_{p_o}(\mathbf{v}; \mathbf{H}_t\mathbf{v}_t, \boldsymbol{\Sigma}_t^o), \end{aligned}$$

and can be solved recursively with the Kalman Filter algorithm described below.

Given the above Gauss-linear model assumptions, the recursive algorithm for computing the forecast is the Kalman Filter (Myrseth & Omre, 2001).

Let $\mathbf{v}_t^u = [\mathbf{v}_t | \mathbf{o}_0, \dots, \mathbf{o}_{t-1}]$ and $\mathbf{v}_t^c = [\mathbf{v}_t | \mathbf{o}_0, \dots, \mathbf{o}_t]$, then the traditional Kalman Filter is given in Algorithm 1.

Algorithm 1 Traditional Kalman Filter

- 1: **Initiate:**
 - 2: $\mathbf{v}_0^u \sim f(\mathbf{v}_0^u) = \phi_{p_u}(\mathbf{v}; \boldsymbol{\mu}_0^u, \boldsymbol{\Sigma}_0^u)$
 - 3: $\boldsymbol{\mu}_0^u = \boldsymbol{\mu}_0^v$
 - 4: $\boldsymbol{\Sigma}_0^u = \boldsymbol{\Sigma}_0^v$
 - 5: **end initiate**
 - 6: **Iterate** $t = 0, \dots, T$
 - 7: Conditioning:
 - 8: $\mathbf{v}_t^c \sim f(\mathbf{v}_t^c) = \phi_{p_u}(\mathbf{v}; \boldsymbol{\mu}_t^c, \boldsymbol{\Sigma}_t^c)$
 - 9: $\boldsymbol{\mu}_t^c = \boldsymbol{\mu}_t^u + \boldsymbol{\Sigma}_t^u \mathbf{H}_t' [\mathbf{H}_t' \boldsymbol{\Sigma}_t^u \mathbf{H}_t' + \boldsymbol{\Sigma}_t^o]^{-1} (\mathbf{o}_t - \mathbf{H}_t \boldsymbol{\mu}_t^u)$
 - 10: $\boldsymbol{\Sigma}_t^c = \boldsymbol{\Sigma}_t^u - \boldsymbol{\Sigma}_t^u \mathbf{H}_t' [\mathbf{H}_t' \boldsymbol{\Sigma}_t^u \mathbf{H}_t' + \boldsymbol{\Sigma}_t^o]^{-1} \mathbf{H}_t \boldsymbol{\Sigma}_t^u$
 - 11: Forwarding:
 - 12: $\mathbf{v}_{t+1}^u \sim f(\mathbf{v}_{t+1}^u) = \phi_{p_u}(\mathbf{v}; \boldsymbol{\mu}_{t+1}^u, \boldsymbol{\Sigma}_{t+1}^u)$
 - 13: $\boldsymbol{\mu}_{t+1}^u = \mathbf{W} \boldsymbol{\mu}_t^c$
 - 14: $\boldsymbol{\Sigma}_{t+1}^u = \mathbf{W} \boldsymbol{\Sigma}_t^c \mathbf{W}^T + \boldsymbol{\Sigma}_t^v$
 - 15: **end iterate**
 - 16: **Forecast:**
 - 17: $f(\mathbf{v}_{T+1}^u | \mathbf{o}_0, \dots, \mathbf{o}_T) = \phi_{p_u}(\mathbf{v}; \boldsymbol{\mu}_{T+1}^u, \boldsymbol{\Sigma}_{T+1}^u)$
 - 18: **end forecast**
-

The Traditional Kalman Filter requires the system to be Gauss-linear. This leads to very fast computations and the ability to find an analytical solution. The requirement of Gauss-linearity does, however, limit the number of systems that can make use of the Kalman Filter.

3.6 Ensemble Kalman Filter

The Ensemble Kalman Filter (EnKF) is an extension of the traditional Kalman Filter and will provide an approximate solution both under Gaussian linearity assumptions and for the nonlinear cases. The difference between the traditional Kalman Filter and the EnKF is the construction of a set of realisations from the initial model. This set of realisations, called an ensemble, is then run through the Kalman Filter and is conditioned upon and adjusted as the realisations are taken through the forward model. The result is a set of approximately independent realisations drawn from $f(\mathbf{v}_T^u | \mathbf{o}_0, \dots, \mathbf{o}_T)$. Let

$$\Sigma_{vo} = \begin{bmatrix} \Sigma_v & \Gamma_{vo} \\ \Gamma_{ov} & \Sigma_o \end{bmatrix}$$

at any time step t . Let $\mathbf{v}_t^u = [\mathbf{v}_t | \mathbf{o}_0, \dots, \mathbf{o}_{t-1}]$ and $\mathbf{v}_t^c = [\mathbf{v}_t | \mathbf{o}_0, \dots, \mathbf{o}_t]$; then the EnKF algorithm is described in Algorithm 2.

The EnKF is a Monte Carlo-based method that can handle nonlinear systems. The method is relatively fast, but will not yield an analytical solution. It needs to be able to restart the forward model at every time step, which is a very complicated operation in our study.

Algorithm 2 Ensemble Kalman Filter

- 1: **Initiate:**
 - 2: $n_e =$ number of ensemble members
 - 3: $\mathbf{v}_0^{u(i)}; i = 1, \dots, n_e$ iid $f(\mathbf{v}_0)$
 - 4: $\boldsymbol{\epsilon}_0^{o(i)} \sim \phi_{p_o}(\boldsymbol{\epsilon}; \mathbf{0}, \mathbf{I}_{p_o}); i = 1, \dots, n_e$
 - 5: $\mathbf{o}_0^{(i)} = \mathbf{H}_t \mathbf{v}_0^{u(i)} + \boldsymbol{\epsilon}_t^{o(i)}; i = 1, \dots, n_e$
 - 6: $\mathbf{e}_0 : \{(\mathbf{v}_0^u, \mathbf{o}_0)^{(i)}; i = 1, \dots, n_e\}$
 - 7: **end initiate**
 - 8: **Iterate** $t = 0, \dots, T$
 - 9: Conditioning:
 - 10: Estimate $\boldsymbol{\Sigma}_{vo}$ from $\mathbf{e}_t \rightarrow \hat{\boldsymbol{\Sigma}}_{vo}$
 - 11: $\mathbf{v}_t^{c(i)} = \mathbf{v}_t^{u(i)} + \hat{\mathbf{\Gamma}}_{vo} \hat{\boldsymbol{\Sigma}}_{vo}^{-1} (\mathbf{o}_t - \mathbf{o}_t^{(i)}); i = 1, \dots, n_e$
 - 12: Forwarding:
 - 13: $\boldsymbol{\epsilon}_t^{v(i)} \sim \phi_{p_v}(\boldsymbol{\epsilon}; \mathbf{0}, \mathbf{I}_{p_v}); i = 1, \dots, n_e$
 - 14: $\mathbf{v}_{t+1}^{u(i)} = \omega(\mathbf{v}_t^{c(i)}) + \boldsymbol{\epsilon}_t^{v(i)}; i = 1, \dots, n_e$
 - 15: $\boldsymbol{\epsilon}_{t+1}^{o(i)} \sim \phi_{p_o}(\boldsymbol{\epsilon}; \mathbf{0}, \mathbf{I}_{p_o}); i = 1, \dots, n_e$
 - 16: $\mathbf{o}_{t+1}^{(i)} = \mathbf{H}_t \omega(\mathbf{v}_{t+1}^{u(i)}) + \boldsymbol{\epsilon}_{t+1}^{o(i)}; i = 1, \dots, n_e$
 - 17: $\mathbf{e}_{t+1} : \{(\mathbf{v}_{t+1}^u, \mathbf{o}_{t+1})^{(i)}; i = 1, \dots, n_e\}$
 - 18: **end iterate**
 - 19: **Assess:**
 - 20: $f(\mathbf{v}_{T+1} | \mathbf{o}_0, \dots, \mathbf{o}_T)$ from \mathbf{e}_{T+1}
 - 21: **end assess**
-

3.7 Particle Filter

When considering nonlinear state estimation problems and non-Gaussian noise, the Particle Filter (PF) is a commonly used method for approximating the posterior. The general idea is to represent the state space PDF as a random set of samples, called particles, instead of as a function over the state space (Gordon et al., 1993). As the number of samples increase, they near the exact state space PDF. This allows for the estimation of moments directly from the samples and the creation of a representation of the PDF (Silverman, 1986).

The earliest mention of the PF is by Gordon et al. (1993), who introduced the idea of representing the state space PDF as samples instead of as a function. Assume we have N random samples from the initial distribution

$$[\mathbf{v}_0^{(1)}, \dots, \mathbf{v}_0^{(N)}] \text{ iid } f(\mathbf{v}_0), \quad (3.9)$$

as described in Section 1.1. The algorithm presented by Gordon et al. (1993) is called the bootstrap filter and is described in Algorithm 3.

Like the EnKF, the PF is a Monte Carlo method. It is an easily implemented and very efficient method for state space estimation. After every resampling step, it needs to restart the forward model. It is not very suitable for parameter estimation, because the resampling does not include the model parameters which remain constant. Moreover, the PF is subject to the curse of dimensionality.

Algorithm 3 Particle Filter

- 1: **Initiate:**
 - 2: N – number of particles
 - 3: Obtain N random samples, $\mathbf{v}_0^{(i)} \sim f(\mathbf{v}_0); i = 1, \dots, N$
 - 4: $w_0^{(i)} = 1/N; i = 1, \dots, N$
 - 5: **end initiate**
 - 6: **Iterate** $t = 1, \dots, T$
 - 7: Forecast $\mathbf{v}_t^{(i)} \sim f(\mathbf{v}_t^{(i)} | \mathbf{v}_{t-1}^{(i)}) = \omega(\mathbf{v}_{t-1}^{(i)}) + \epsilon_t; i = 1, \dots, N.$
 - 8: **Update weights:**
 - 9: $w_t^{(i)} = f(\mathbf{o}_t | \mathbf{v}_t^{(i)}) w_{t-1}^{(i)} / \sum_{j=1}^N f(\mathbf{o}_t | \mathbf{v}_t^{(j)}) w_{t-1}^{(j)}$
 - 10: **end update**
 - 11: **Assess:**
 - 12: $f(\mathbf{v}_t | \mathbf{o}_0, \dots, \mathbf{o}_t)$ from $\{(\mathbf{v}_t^{(i)}, w_t^{(i)}); i = 1, \dots, N\}$
 - 13: **end assess**
 - 14: **if** $\{w_t^{(i)}; i = 1, \dots, N\}$ too dispersed **then** resample:
 - 15: $\mathbf{v}_t^{(b)} \sim \text{Multinomial}[\mathbf{v}_t^{(1)}, \dots, \mathbf{v}_t^{(N)}; w_t^{(1)}, \dots, w_t^{(N)}]; b = 1, \dots, N$
 - 16: $w_t^{(b)} = 1/N; b = 1, \dots, N$
 - 17: **end if**
 - 18: **end iterate**
-

3.8 Parameter Particle Filter

Because the system in question is nonlinear, the Traditional Kalman Filter is not very suitable. And because it is quite difficult to restart the forward model, the EnKF becomes difficult to use. This study focuses on the model parameter, $\boldsymbol{\lambda}$, which makes the regular PF unsuitable. Instead, we define a version of the PF such that the assessment of the model parameters can be made.

First, N particles are drawn from the initial distribution, $\mathbf{u}_0^{(i)} = \mathbf{u}_0; i = 1, \dots, N$, with respective initial parameters, $\boldsymbol{\lambda}_0^{(i)} \sim f(\boldsymbol{\lambda}); i = 1, \dots, N$. For each time step, the normalised weights are found. The effective sample size is a measure of how dispersed the particles are, and if it is below a threshold value, we perform the perturbation. First, we find the empirical covariance matrix of \mathbf{v}_t and identify which particles have weights above a given threshold. Then, the particles with weights below the given thresh-

old are discarded and new particles are centred around the kept particles. The distance between the new and the retained particles is determined by the empirical covariance matrix, which is scaled such that the new distribution of particles is close to the particles that were retained. Then, a parameter update of $\boldsymbol{\lambda}$ is performed using an ensemble Kalman update for the perturbed particles. The weights are all set equal to $1/N$, because we have no information about the new distribution. Below is the algorithmic representation of the Parameter Particle Filter.

Algorithm 4 Parameter Particle Filter

- 1: **Initiate:**
 - 2: N – number of particles
 - 3: $\mathbf{u}_0^{(i)} = \mathbf{u}_0; i = 1, \dots, N$
 - 4: $\boldsymbol{\lambda}_0^{(i)} \sim f(\boldsymbol{\lambda}); i = 1, \dots, N$
 - 5: $\mathbf{v}_0^{(i)} = \begin{bmatrix} \mathbf{u}_0^{(i)} \\ \boldsymbol{\lambda}_0^{(i)} \end{bmatrix}; i = 1, \dots, N$
 - 6: $w_0^{(i)} = 1/N; i = 1, \dots, N$
 - 7: $\mathbf{e}_0 = \{(\mathbf{v}_0^{(i)}, w_0^{(i)}); i = 1, \dots, N\}$
 - 8: **end initiate**
 - 9: **Run forward model:**
 - 10: $\mathbf{v}_t^{(i)} = \begin{bmatrix} \mathbf{u}_t^{(i)} \\ \boldsymbol{\lambda}_t^{(i)} \end{bmatrix} = \begin{bmatrix} \omega(\mathbf{u}_{t-1}^{(i)}, \boldsymbol{\lambda}_{t-1}^{(i)}) \\ \boldsymbol{\lambda}_{t-1}^{(i)} \end{bmatrix}; i = 1, \dots, N$
 - 11: **end forward model**
 - 12: **Iterate**
 - 13: $cpt = 0$
 - 14: **Iterate** $s = 1, \dots$
 - 15: $tt = cpt + s$
 - 16: **if** $tt > T$ **then** STOP;
 - 17: **end if** ▷ Algorithm 4 to be continued
-

Algorithm 4 Parameter Particle Filter (continued)

```

18:    $w_{tt}^{(i),*} = f(\mathbf{o}_{tt}|\mathbf{v}_{tt}) \times w_{tt-1}^{(i)}, i = 1, \dots, N$ 
19:    $w_{tt}^{(i)}$  – normalised weights
20:   Define  $\mathbf{e}_{tt} : \{(\mathbf{v}_{tt}^{(i)}, w_{tt}^{(i)}); i = 1, \dots, N\}$ 
21:    $N_{eff} = [\sum_i (w_{tt}^{(i)})^2]^{-1}$ 
22:   if weights too dispersed then perturb
23:   end if
24:   Perturb:  $[\mathbf{u}, \boldsymbol{\lambda}]$ 
25:     Estimate  $\boldsymbol{\Sigma}_{u\lambda}^{tt}$  from  $\mathbf{e}_{tt} \rightarrow \hat{\boldsymbol{\Sigma}}_{u\lambda}^{tt}$ 
26:     Identify index  $i$  in  $\mathbf{e}_{tt}$  with  $w_{tt}^{(i)} > w^R \rightarrow \mathcal{I}_p$ 
27:     for  $j \in \mathcal{I}_p$  do
28:       Identify  $n_p^{(j)} \propto w_{tt}^{(j)}$  s.t  $N = \sum_j n_{tt}^{(j)}$ 
29:     end for
30:     for  $j \in \mathcal{I}_p$  do
31:        $\mathbf{u}_{tt+l}^{(j),1} = \mathbf{u}_{tt+l}^{(j)}; l = 0, \dots, T - tt$ 
32:        $\boldsymbol{\lambda}_{tt+l}^{(j),1} = \boldsymbol{\lambda}_{tt+l}^{(j)}; l = 0, \dots, T - tt$ 
33:     end for
34:     Perturbate  $\mathbf{u}_{tt}^{(j)}$   $n_j^p$  times:
35:     for  $k = 2, \dots, n_j^p$  do
36:        $\boldsymbol{\epsilon}_u \sim f(\boldsymbol{\epsilon}) = \phi(\boldsymbol{\epsilon}; \mathbf{0}, \tau \hat{\boldsymbol{\Sigma}}_u^{tt})$ 
37:        $\mathbf{u}_{tt+l}^{(j),k} = \mathbf{u}_{tt+l}^{(j)} + \boldsymbol{\epsilon}_u; l = 0, \dots, T - tt$ 
38:        $\boldsymbol{\lambda}_{tt+l}^{(j),k} = \boldsymbol{\lambda}_{tt+l}^{(j)} + \hat{\boldsymbol{\Gamma}}_{\lambda,u}^{tt} [\hat{\boldsymbol{\Sigma}}_u^{tt}]^{-1} \boldsymbol{\epsilon}_u; l = 0, \dots, T - tt$ 
39:     end for
40:   end perturb
41:   Copy  $\begin{bmatrix} \mathbf{u}_{tt}^{(j),k} \\ \boldsymbol{\lambda}_{tt}^{(j),k} \end{bmatrix}; j \in \mathcal{I}_p, k = 1, \dots, n_j^p$  into  $\mathbf{v}_{tt+l}^{(i)}; l = 0, \dots, T - tt$ 
42:    $w_{tt}^{(i)} = 1/N; i = 1, \dots, N$ 
43:    $cpt = tt$ 
44:   end iterate
45: end iterate

```

Like the traditional version of the PF, this version is based on a Monte Carlo approach. Normally, the PF would predict the next state space at each time step, but here the forward model is run only once. The state space is instead updated through random shifts in the temperature profiles when we perturb. When the weights become too dispersed, the particles with low weights are discarded and perturbed around the particles with high weights. This is done by shifting the new particles from the retained particles by ϵ_u with a zero-mean PDF with scaled empirical covariance matrix, $\epsilon_u \sim \phi(\epsilon; \mathbf{0}, \tau \hat{\Sigma}_u)$. The scaling factor, τ , is used to ensure the new particles are generated close to the retained particles. To update the state space, the new temperature profiles are shifted around the kept temperature profiles by ϵ_u and letting them run parallel to each other.

The Parameter Particle Filter also implements a parameter estimation of λ using empirical regression into the λ -space. This is done by an Ensemble Kalman update using ϵ_u at every perturbation. It is a very efficient algorithm, and in the case study, we will evaluate it on the ice-pad example and estimate the heat transfer coefficient, λ , of the ice pad.

Chapter 4

Case Study

We apply our PF to an ice rink floor, in order to estimate the thermal conductivity, $\boldsymbol{\lambda}$, using synthetic data. The floor of the ice rink is composed of three layers: ice, concrete and insulation. Each component has a different heat transfer coefficient, which we will find using parameter estimation. The initial conditions for the temperature, $\mathbf{u}(\mathbf{x}, 0)$, are displayed in Figure 2.7 and we generate $\boldsymbol{\lambda}^{(i)}; i = 1, \dots, N$ from the prior $\phi_3(\boldsymbol{\lambda}; \hat{\boldsymbol{\lambda}}, \hat{\boldsymbol{\sigma}}_\lambda)$, which is right-shifted relative to $\boldsymbol{\lambda}^{(ref)}$, as the initial distribution of $\boldsymbol{\lambda}$, where $\hat{\boldsymbol{\lambda}} = (2.5, 1.2, 0.004)$, $\hat{\boldsymbol{\sigma}}_\lambda = (1.2, 1.2, 0.001)$ and $N = 50$. We run the forward model once to compute $\mathbf{v}_t^{(i)} = \begin{bmatrix} \mathbf{u}_t^{(i)} \\ \boldsymbol{\lambda}^{(i)} \end{bmatrix}; i = 1, \dots, N; t = 1, \dots, T$, because we cannot restart the forward model when running the Parameter Particle Filter. The scaling parameter, τ , is set to $\tau = 0.1$.

We start by displaying the synthetic data along with the temperature distribution of four randomly drawn particles. Then, we display the weights and the empirical parameter distributions, and lastly, we discuss the results of the case study.

4.1 Synthetic Data

Due to difficulties and time constraints, real observations of the temperature are not available for this study, and synthetic data will be used instead. The synthetic data are created by running the temperature simulations in COMSOL using the reference value $\boldsymbol{\lambda}^{(ref)} = (2.25, 1.00, 0.0030)$ and then adding a Gaussian error term, $\boldsymbol{\epsilon}_t \sim \phi_4(\boldsymbol{\epsilon}; \mathbf{0}, \hat{\boldsymbol{\Sigma}})$. The synthetic data are given in Figures 4.1, 4.2, 4.3 and 4.4, for each of the four observed positions.

All particles are fairly close to the synthetic data, with particle 9 being the closest. Particle 9's heat transfer coefficient, $\boldsymbol{\lambda}^{(9)} = (2.37, 1.00, 0.0030)$, is very close to the reference value, $\boldsymbol{\lambda}^{(ref)}$, whereas the other particles exhibit a greater difference from the reference value. Because the sides and bottom have constant boundary conditions at $0^\circ C$ and the cooling pipes have constant temperature at $-6^\circ C$ and $-8^\circ C$ for the inbound and outbound pipes, respectively, the temperature simulated between the pipes (at position T5) is lower than near the boundary (positions T6, T7). The ice pad is the warmest layer, because it is not insulated from the heat flux from the indoor air, which has a temperature of $+4^\circ C$. This shows that there is a noticeable difference in the temperature distributions due to the difference in the value of the heat transfer coefficients.

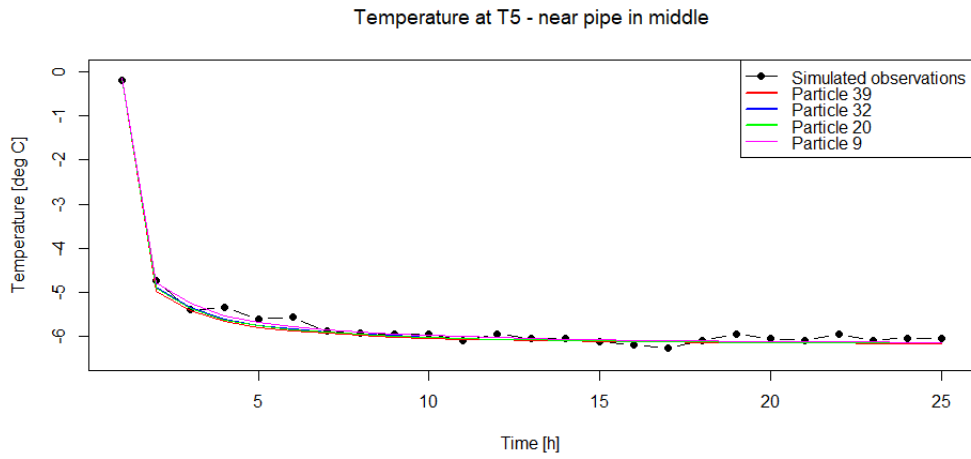


Figure 4.1: Temperature distribution in the middle of the cooling pipes of four particles and the synthetic data.

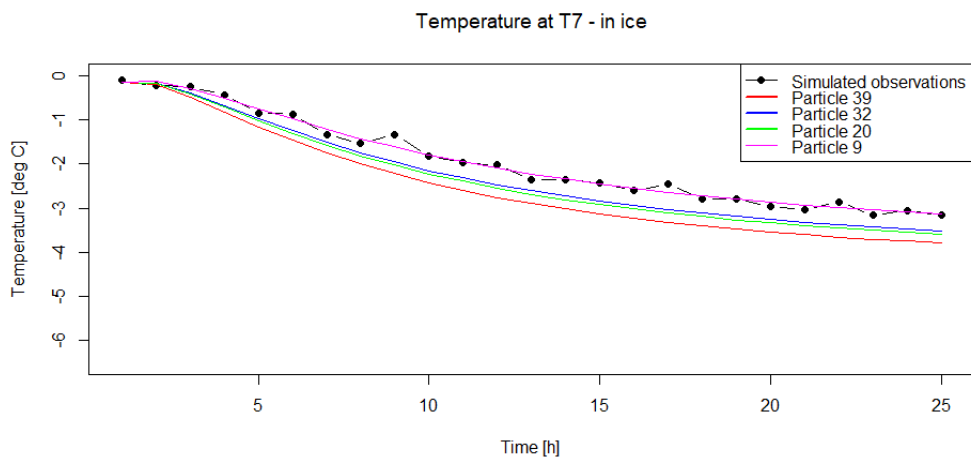


Figure 4.2: Temperature distribution in the ice pad of four particles and the synthetic data.

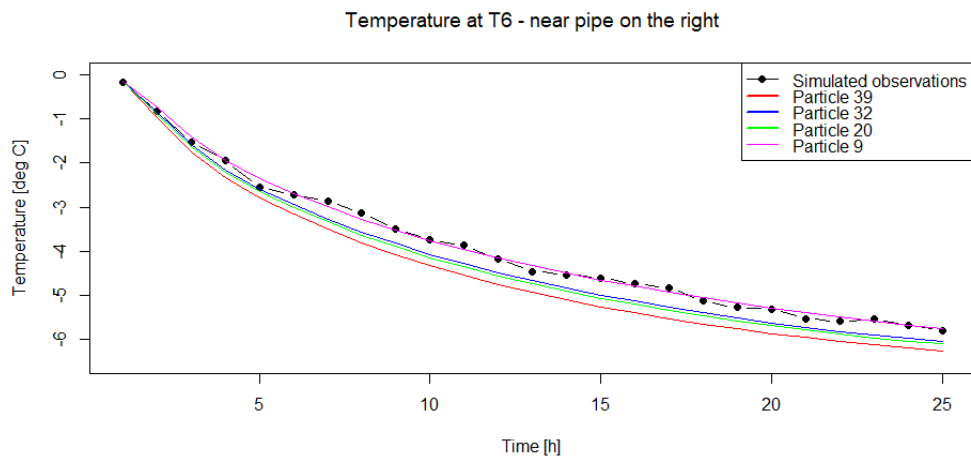


Figure 4.3: Temperature distribution to the right of the cooling pipes of four particles and the synthetic data.

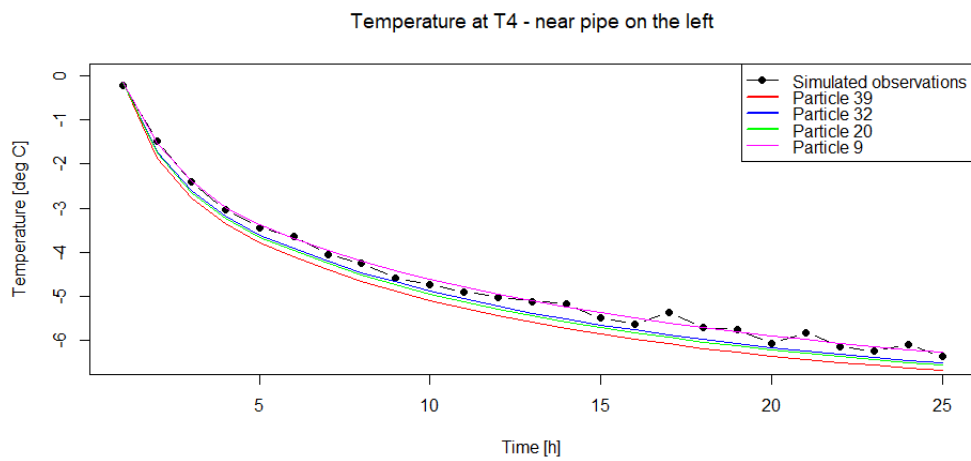


Figure 4.4: Temperature distribution to the left of the cooling pipes of four particles and the synthetic data.

4.2 Weight Distribution

We use $N = 50$ in our study with no restart of the forward model. The corresponding weights will vary with time due to conditioning. Figure 4.5 shows the distribution of the weights for $t = 0, 1$. Initially, all weights are equal, $w_i = 1/N$; $i = 1, \dots, N$, because there are no observations available with which to determine which particles have the best fit. When $t = 1$, only eight particles have weights around or higher than $1/N = 0.02$. The weights are now too dispersed and the particles with low weights are discarded, and perturbations are made around the particles with higher weights. The effective sample size (ESS) at $t = 1$ was $\text{ESS}_1 = 6.8$, which is well below the threshold of $N^* = 37$ chosen for this case study. After perturbing, all particles are given equal weight, since they are all distributed around the previous high-weighted particles, as illustrated in Figure 4.6.

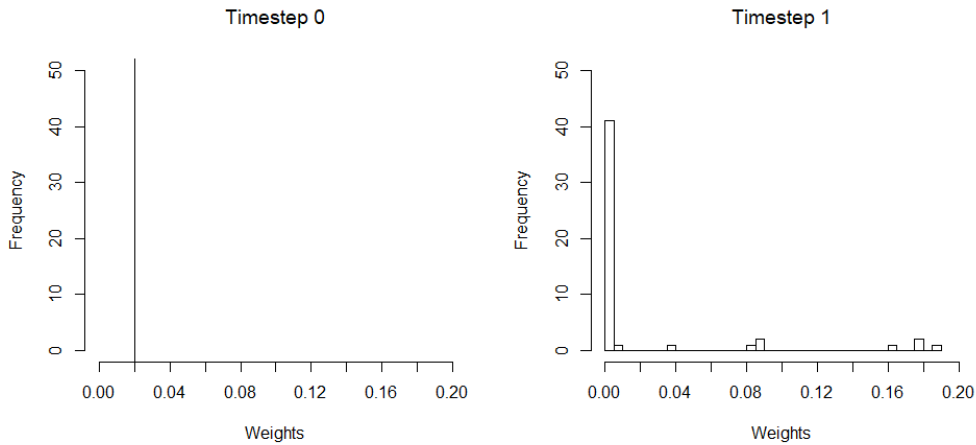


Figure 4.5: Distribution of the weights at $t = 0, 1$.

At $t = 3, 4$, the weights are slowly spreading out from $1/N$ until $t = 5$, where $\text{ESS}_5 = 32$, indicating the weights are too dispersed, as illustrated in Figures 4.6 and 4.7. After perturbing at $t = 5$, all particles have equal weight, as shown in Figure 4.7.

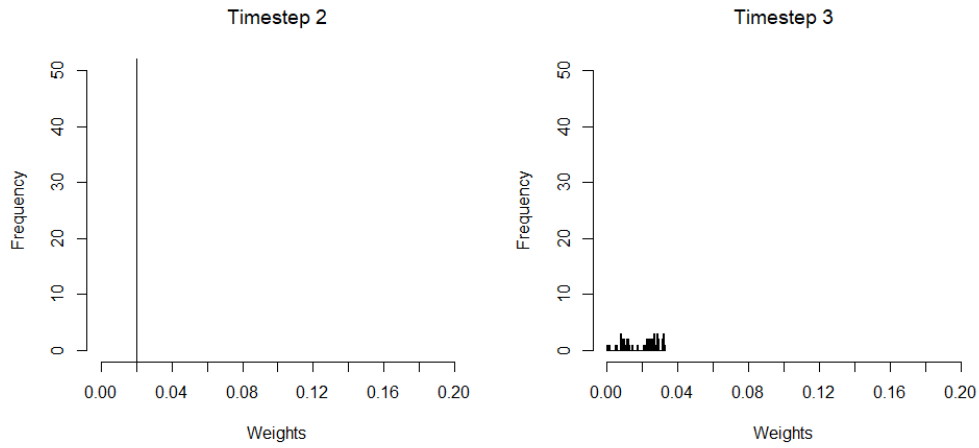


Figure 4.6: Distribution of the weights at $t = 2, 3$.

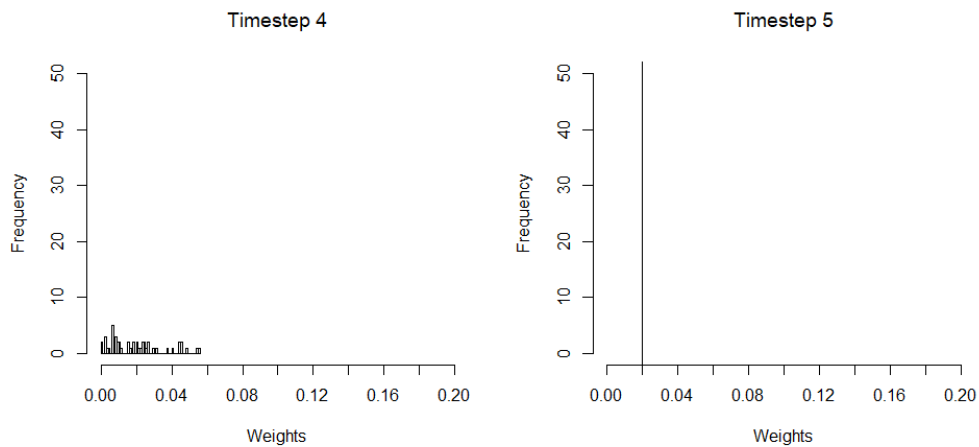


Figure 4.7: Distribution of the weights at $t = 4, 5$.

4.2. WEIGHT DISTRIBUTION

Figures 4.8 and 4.9 show the distribution of the weights for $t = 6, 7$ and $t = 8, 9$, respectively. The weights are again slowly spreading out from $1/N$, but not as quickly as before. This indicates that the fit of the particles is improving.

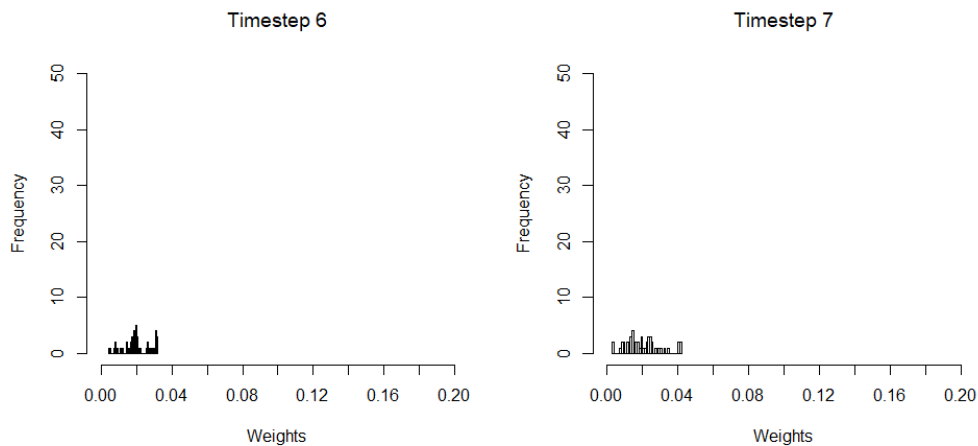


Figure 4.8: Distribution of the weights at $t = 6, 7$.

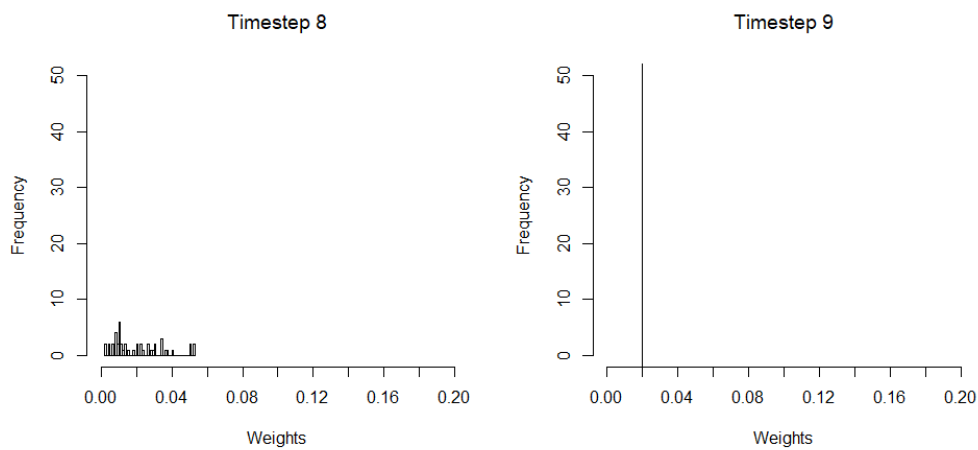


Figure 4.9: Distribution of the weights at $t = 8, 9$.

At $t = 9$, the weights have become too dispersed again, and we perturb, as shown in Figure 4.9. For $t = 10, \dots, 15$, the weights are very slowly spreading out from $1/N$, as illustrated in Figures 4.10, 4.11 and 4.12. This time, there are fewer particles with higher weights. Most particles are spread closely around $1/N$, indicating that the fit of the particles is continuing to improve. The last perturbation happens at $t = 16$, as shown in Figure 4.13 and for $t = 17, \dots, 24$, almost all weights are equal to $1/N$, with $\text{ESS}_{25} = 48.8$, shown in Figures 4.14, 4.15 and 4.17.

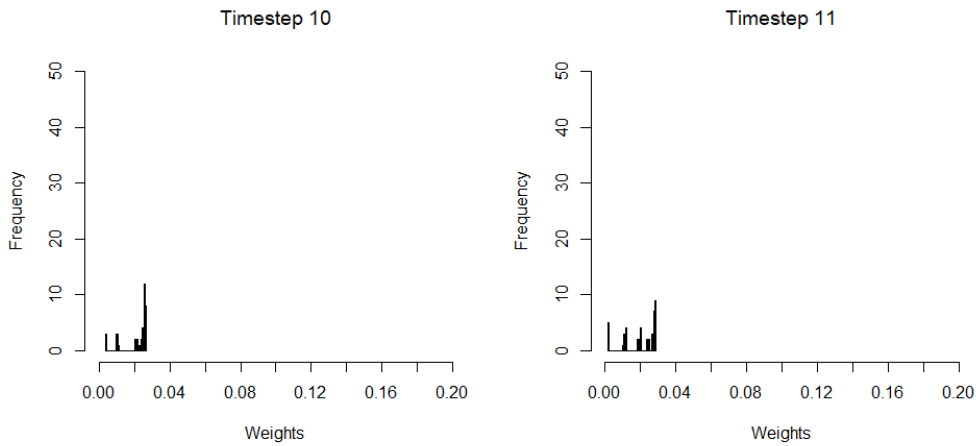


Figure 4.10: Distribution of the weights at $t = 10, 11$.

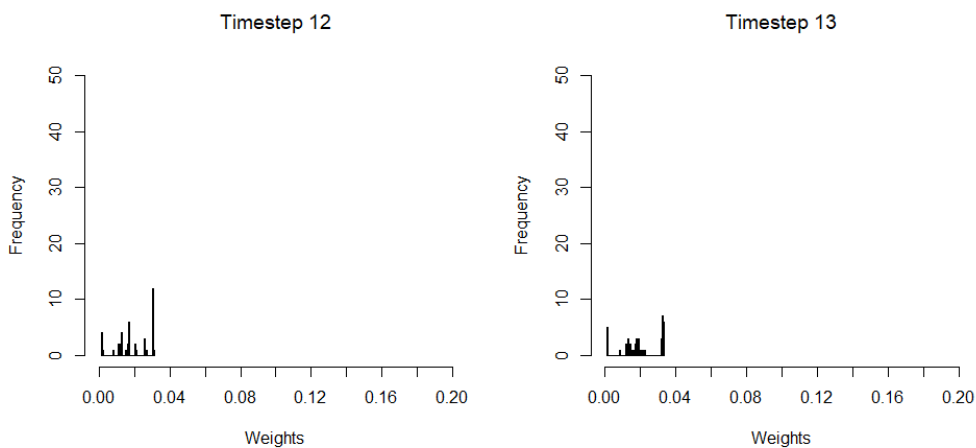


Figure 4.11: Distribution of the weights at $t = 12, 13$.

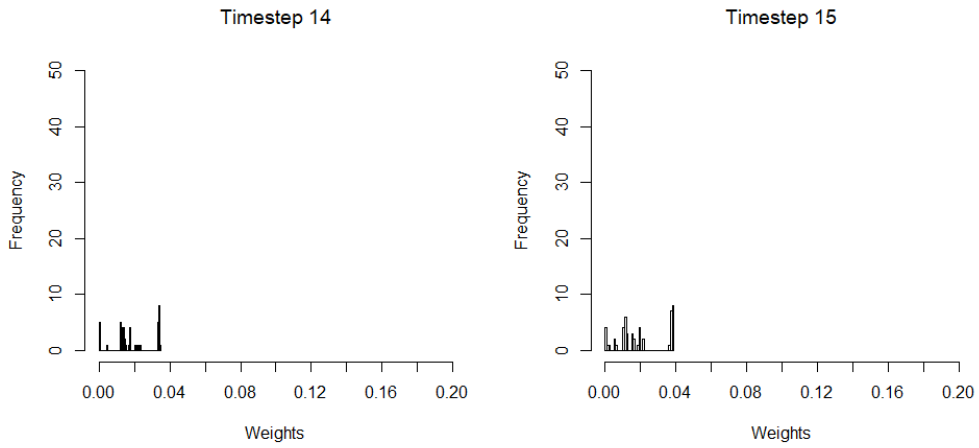


Figure 4.12: Distribution of the weights at $t = 14, 15$.

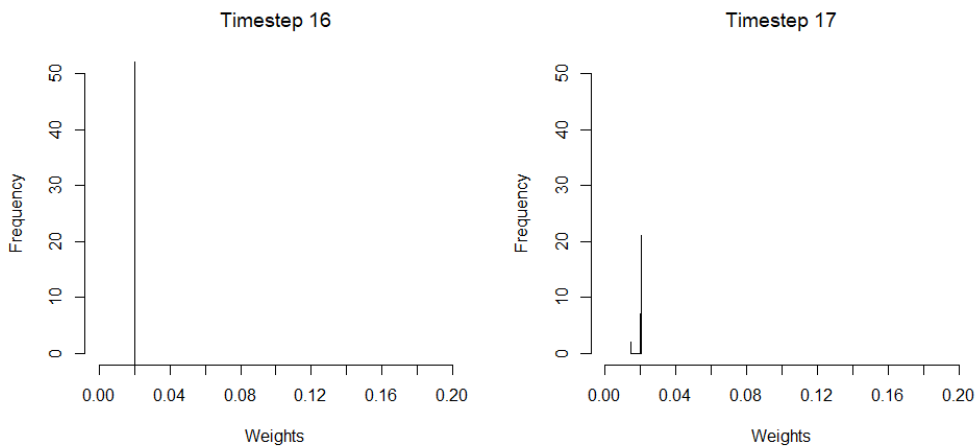


Figure 4.13: Distribution of the weights at $t = 16, 17$.

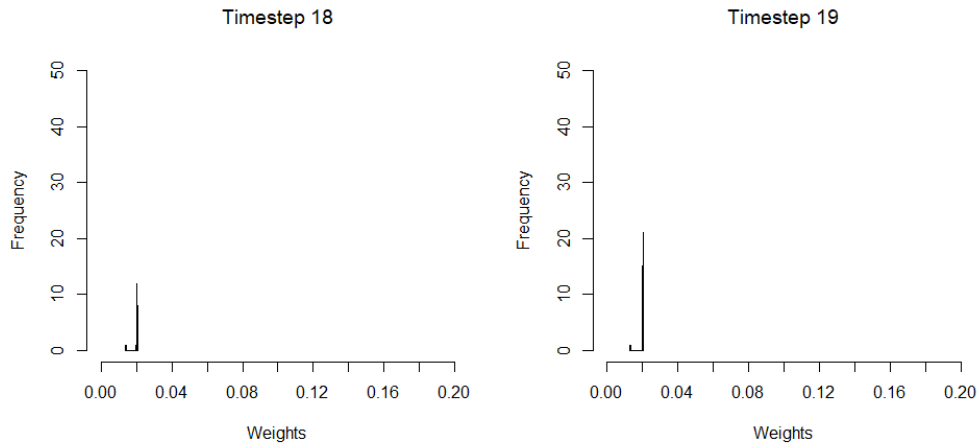


Figure 4.14: Distribution of the weights at $t = 18, 19$.

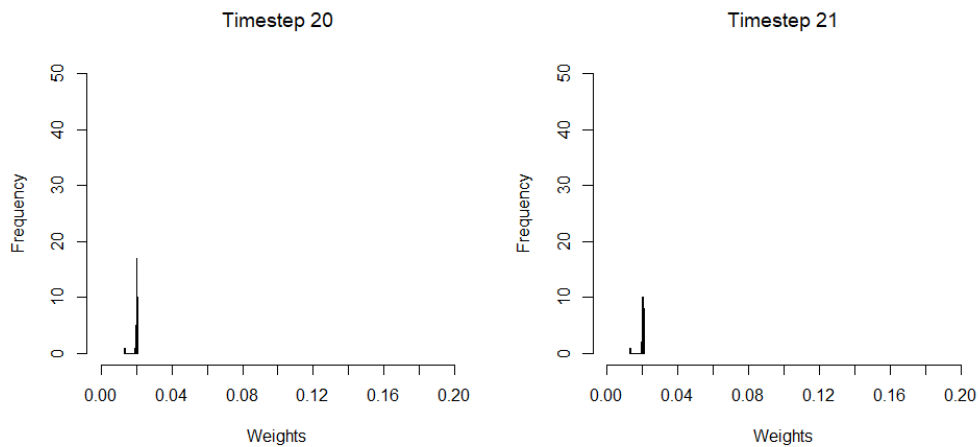
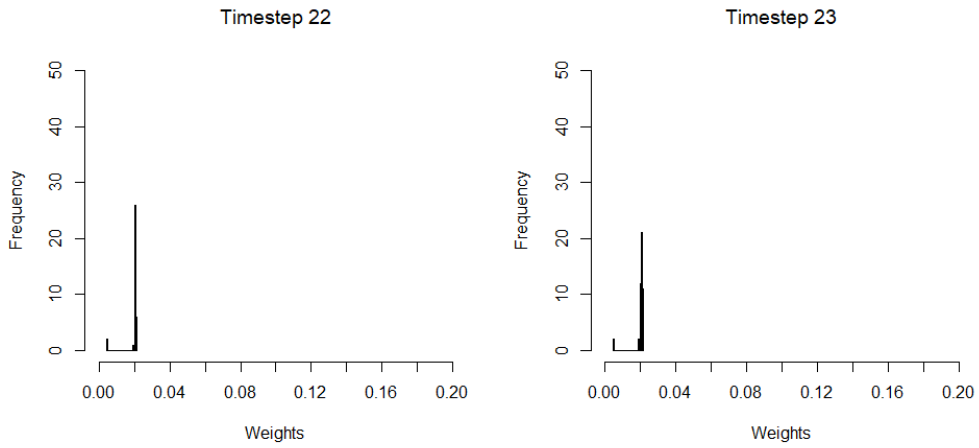
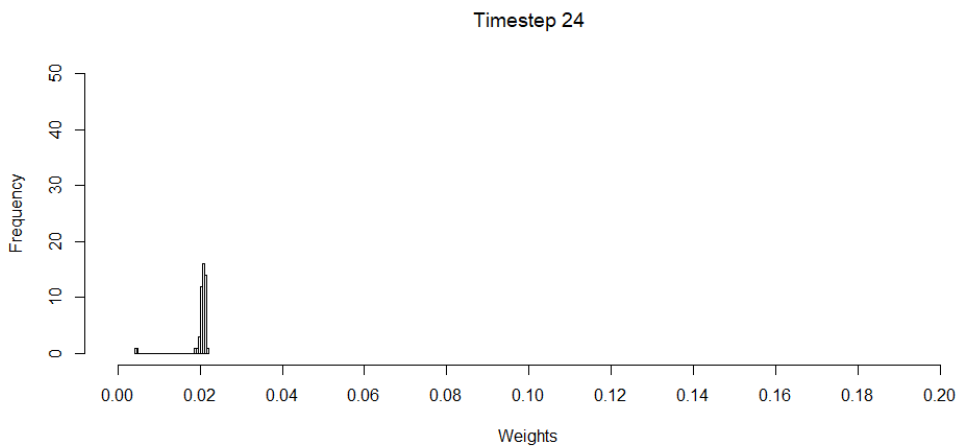


Figure 4.15: Distribution of the weights at $t = 20, 21$.

Figure 4.16: Distribution of the weights at $t = 22, 23$.Figure 4.17: Distribution of the weights at $t = 24$.

4.3 Empirical Model Parameter Distribution

The initial distribution of λ is shown in Figure 4.18. Here, the distributions are intentionally right-shifted Gaussian, with the red vertical line indicating the reference values for λ . The reason for this is to simulate a bad initial guess of the parameter.

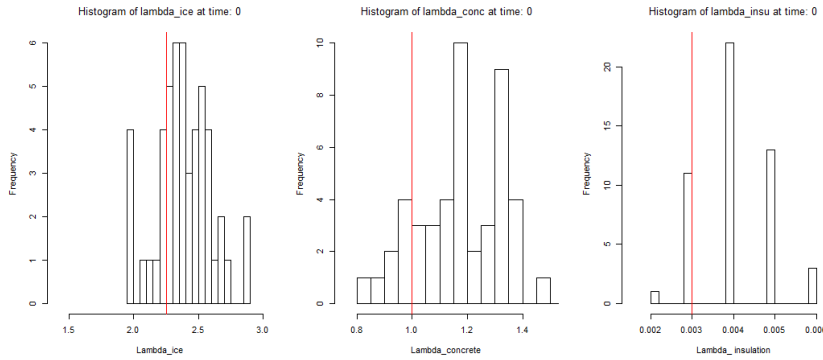


Figure 4.18: Initial distribution of λ .

After the first perturbation at $t = 1$, the width of the distributions for the concrete and insulation parameter has narrowed. They have also become centred more around the reference values. For ice, the distribution is the same width, although it has lost its Gaussian shape, as shown in Figure 4.19.

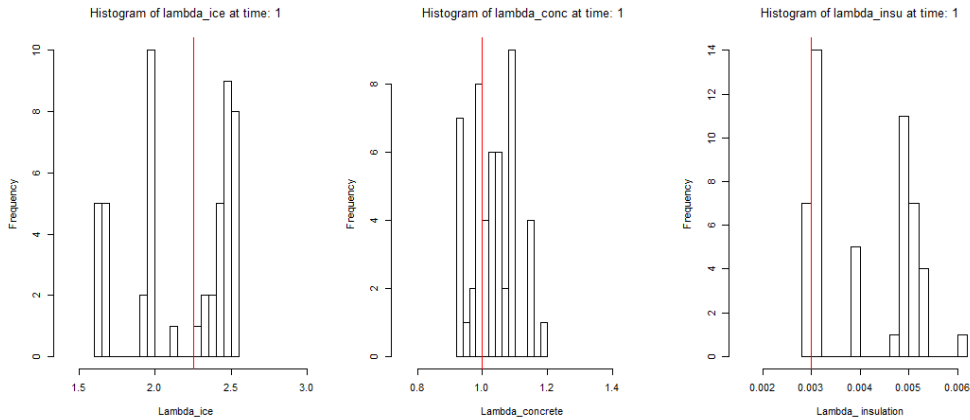


Figure 4.19: Distribution of λ after the first perturbation at $t = 1$.

4.3. EMPIRICAL MODEL PARAMETER DISTRIBUTION

Figure 4.20 shows the distributions after the second perturbation. The concrete parameter has improved significantly. Its distribution has become more narrow and centred around the reference value. The distribution for the insulation parameter has narrowed somewhat, but is still right-shifted. There is no significant change in the ice parameter.

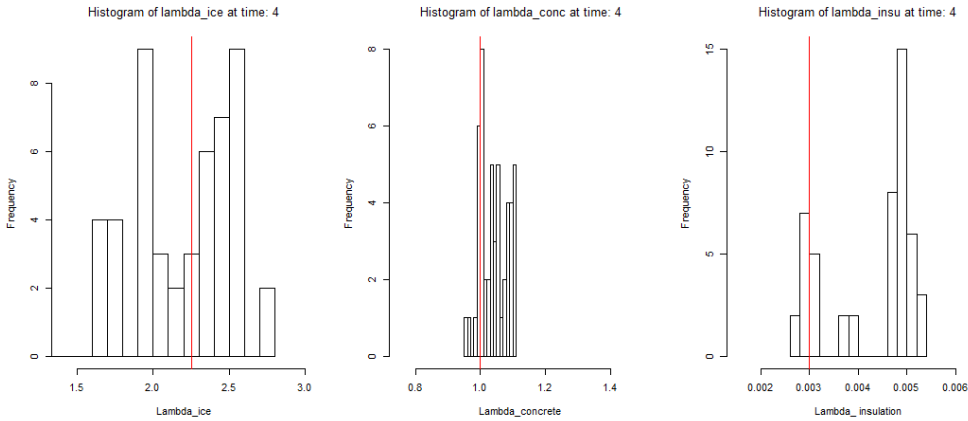


Figure 4.20: Distribution of λ after the second perturbation at $t = 4$.

The distributions after the third perturbation are shown in Figure 4.21. For the ice parameter, the centring is closer to the reference values, although still slightly right-shifted. The concrete parameter is mostly unchanged, and the insulation parameter is correctly centred but is still distributed widely.

Figure 4.22 shows the distributions after the fourth and final perturbation. The distributions for both the concrete and insulation parameters have narrowed significantly and centred around the reference values. For the ice parameter, the distribution has narrowed somewhat, with most of the particles being slightly right-shifted in relation to the reference value. Figure 4.23 shows the final weighted distributions at $t = 24$, which are very similar to the distributions after the last perturbation, as shown in Figure 4.22.

CHAPTER 4. CASE STUDY

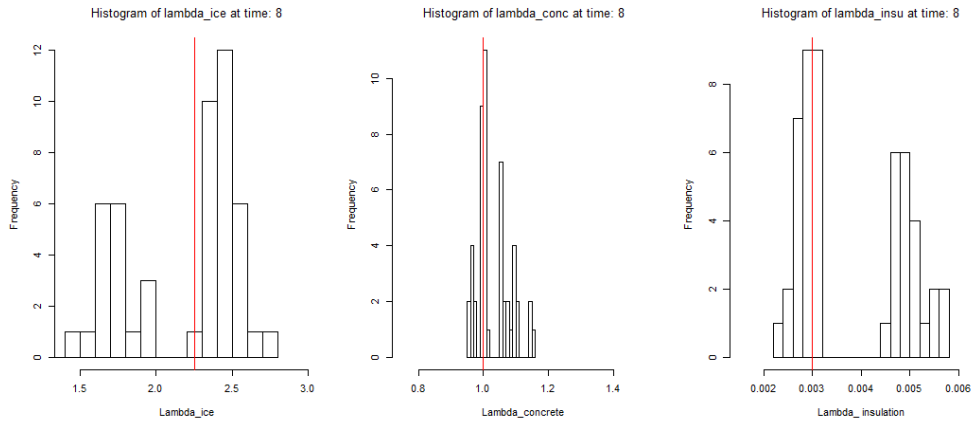


Figure 4.21: Distribution of λ after the third perturbation at $t = 8$.

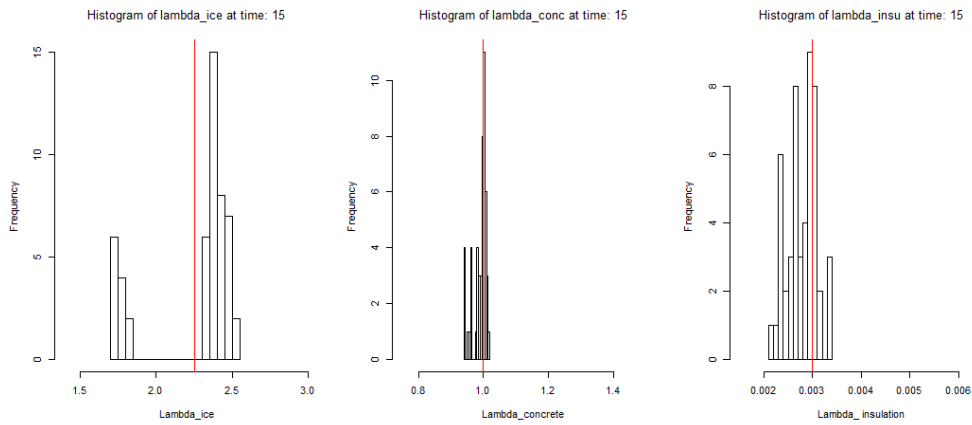


Figure 4.22: Distribution of λ after the fourth and last perturbation at $t = 15$.

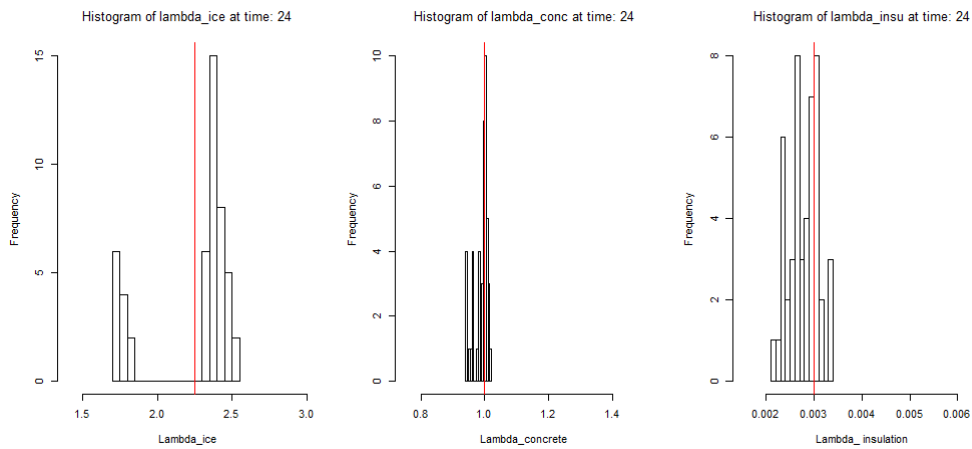


Figure 4.23: Distribution of λ at $t = 24$.

4.4 Discussion of the Test Case

The histograms of the weights and λ show promising results. In the beginning, only a few particles are high-weighted, which indicates that a few particles have good fit, whilst the majority is far off. After perturbing, the weight distribution is mostly even around $1/N$ and the parameter distributions for both concrete and insulation have narrowed and centred more around the reference value. This trend continues; after each perturbation, the weight distribution remains centred around $1/N$ longer before spreading out, and in the final time steps, almost all particles have weight $1/N$, as illustrated in Figure 4.17.

There is also an improvement to the empirical distribution of λ . Initially, the empirical distribution is wide and right-shifted. After each perturbation, the distributions get more narrow and centred around the reference value. The empirical distribution for the ice parameter is still somewhat right-shifted and has a few particles to the left of the reference value. However, the general trend is that the empirical distribution narrows and the centring moves towards the reference value.

Table 4.1 presents the mean and the mean square error of λ , here denoted $\mu_\lambda|\kappa$ and $s|\kappa$, respectively. They are displayed at $t = 0$, after each perturbation and at the end of the simulations. The table shows that the MSE is fairly low and decreases with each perturbation. The mean nears the reference values at each perturbation and ultimately settles almost perfectly at the reference values. For $t = 24$, we have the weighted mean and mean square error.

Table 4.1: The mean and MSE of λ at each perturbation, with $\lambda^{(ref)} = (2.25, 1, 0.003)$.

	$t = 0$	$t = 1$	$t = 4$	$t = 8$	$t = 15$	$t = 24$
$\mu_\lambda \kappa = \text{ice}$	2.39	2.17	2.18	2.16	2.25	2.24
$\mu_\lambda \kappa = \text{conc}$	1.21	1.03	1.04	1.03	0.99	0.99
$\mu_\lambda \kappa = \text{insu}$	0.00412	0.0041	0.0043	0.0038	0.0028	0.0028
$s \kappa = \text{ice}$	1.92×10^{-2}	6.23×10^{-3}	4.55×10^{-3}	7.31×10^{-3}	4.92×10^{-7}	1.58×10^{-4}
$s \kappa = \text{conc}$	4.42×10^{-2}	1.12×10^{-3}	1.71×10^{-3}	9.28×10^{-4}	9.79×10^{-5}	1.98×10^{-4}
$s \kappa = \text{insu}$	1.25×10^{-6}	1.20×10^{-6}	1.65×10^{-6}	6.55×10^{-7}	4.46×10^{-8}	5.02×10^{-8}

Figures 4.24, 4.25 and 4.26 display the empirical confidence intervals for λ . The red line in the figures represents the reference values of the respective heat transfer coefficients. These intervals are created by removing the two smallest and two largest particles in each time step and centring the intervals around the average values, represented by the black dots. Figures 4.24, 4.25 and 4.26, show an immediate narrowing of the interval for both the concrete and insulation parameters. The concrete parameter also shifts its average towards the reference value, as does the ice parameter. After the last perturbation, the intervals of the concrete and insulation parameters are very narrow and the average values are quite near the reference values. As for the ice parameter, the interval is slightly narrowed, but the average value is very near the reference value.

4.4. DISCUSSION OF THE TEST CASE

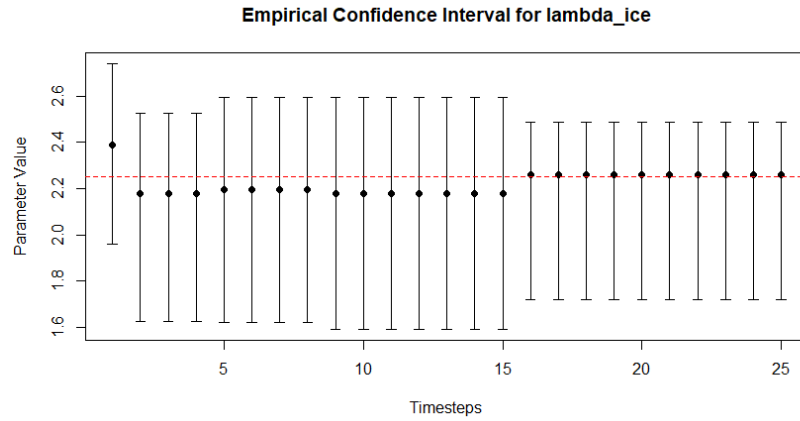


Figure 4.24: Empirical confidence interval for the heat transfer coefficient of ice.

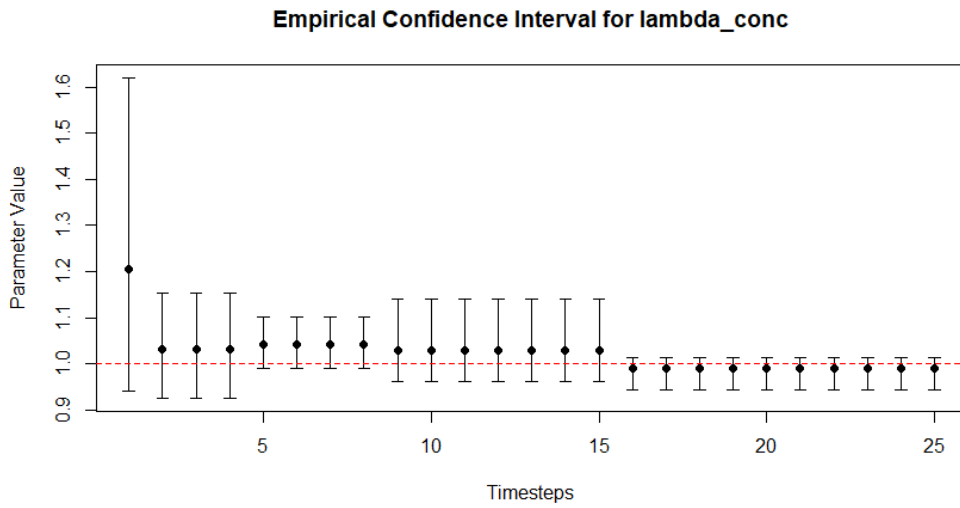


Figure 4.25: Empirical confidence interval for the heat transfer coefficient of concrete.

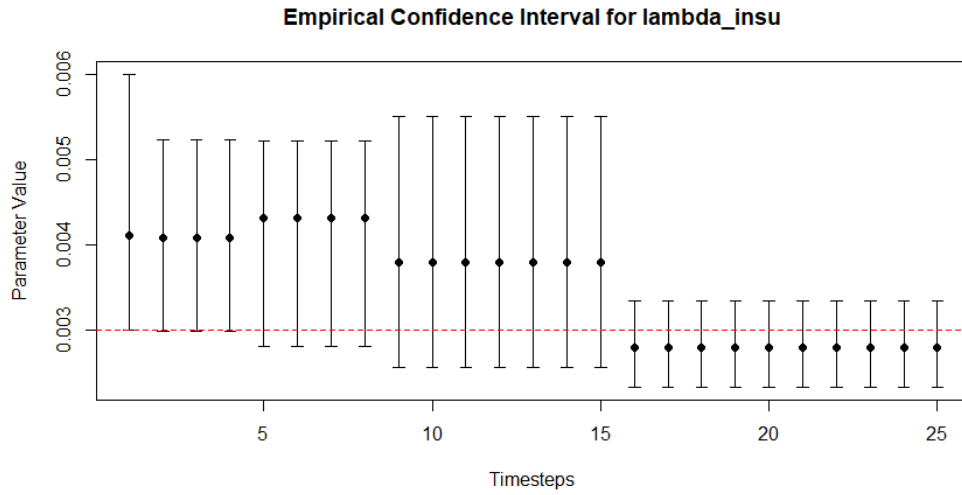


Figure 4.26: Empirical confidence interval for the heat transfer coefficient of insulation.

The results shown in the development of the empirical distributions of λ , the weight distributions and the empirical confidence intervals, indicate that the PF is able to successfully estimate the thermal conductivity of the three layers of the ice rink floor.

Chapter 5

Closing Remarks

In this study, the Parameter Particle Filter, a Particle Filter with parameter updating for estimation of site-specific thermal parameters, is presented. A numerical scheme is developed for the transient heat conduction and simulated using the computer software COMSOL. The traditional Kalman Filter is considered, but it is not applicable, because the system in question is nonlinear. Because the forward model can not be restarted, both the Ensemble Kalman Filter and the traditional Particle Filter are difficult to use. The temperature profiles are resampled and perturbed and the parameter updating is done using an estimated Kalman update. Using synthetic data, the Particle Filter developed in this study is tested on the thermal conductivity parameter of an ice rink floor.

The Parameter Particle Filter quite precisely estimates reference value of the thermal conductivity for both the concrete and insulation layer of the ice rink floor. Starting with a right-shifted and wide distribution, the Parameter Particle Filter centres the estimated parameter distributions around the reference values and narrows the widths of the estimated distributions. The narrowing of the empirical distributions is due to the

empirical covariance matrix being scaled by the scaling parameter during perturbation. This ensures that the new particles are distributed close to the particles with a good fit. For the thermal conductivity of the ice pad, the width of the estimated distribution is still somewhat wide and slightly right-shifted, but the mean is very close to the reference value.

Judging by the results, the Parameter Particle Filter developed in this study successfully estimates the thermal conductivity of an ice rink floor. The method is computationally efficient and very fast. It has the added benefit of only needing to run the forward model once. The Particle Filter can easily be expanded to handle multiple parameters, but it is subject to the curse of dimensionality.

Future work could incorporate this method as an analytical tool in construction when considering what materials to use. The Parameter Particle Filter can provide valuable information regarding which material composition will provide the desired temperature distribution. In ice rinks, this aspect of temperature control is vital in order to maximise energy saving.

Bibliography

Alspach, D., & Sorenson, H. (1972). Nonlinear bayesian estimation using gaussian sum approximations. *IEEE Transactions on Automatic Control*, 17(4), p. 439-448.

Bergheau, J.-M. (2010). *Finite element simulation of heat transfer*. Wiley.

DeWitt, K. J., & Baliga, G. (1982). Numerical simulation of one-dimensional heat transfer in composite bodies with phase change - nasa-cr-165607. *NASA Center for AeroSpace Information (CASI)*, 78, p. 571-587.

Ferrantelli, A., & Viljanen, K. (2015). Heat transfer in ice hockey halls: measurements, energy analysis and analytical ice pad temperature profile. *Cornell University Library*.

Gonzalez, F. (2002). Ice rink guide. *International Ice Hockey Federation*.

Gordon, N., Salmond, D., & Smith, A. (1993). Novel approach to nonlinear/non-gaussian bayesian state estimation. *IEE Proceedings*, 140, p. 107-113.

Gustafsson, F. (2010). Particle filter theory and practice with positioning applications. *IEEE Aerospace and Electronic Systems Magazine*, 25, p. 53-82.

BIBLIOGRAPHY

- Han, D., Nie, H., Chen, M., & Wang, X. (2015). Temperature prediction with humanoid finger sensor based on fourier's law. *IOP Science*.
- Julier, S., Uhlmann, J., & Durrant-Whyte, H. (1995). A new approach for filtering nonlinear systems. In *Proceedings of 1995 American Control Conference - ACC'95*, 73, p. 1628-1632.
- Kalman, R. (1960). A new approach to linear filtering and prediction problems. *Journal of Basic Engineering*.
- Kramer, S. C., & Sorenson, H. W. (1988). Recursive bayesian estimation using piece-wise constant approximations. *Automatica*, 24(6), p. 789-801.
- Mun, J., & Krarti, M. (2011). An ice rink floor thermal model suitable for whole-building energy simulation analysis. *Building and Environment*, 46, p. 1087-1093.
- Mun, J., & Krarti, M. (2015). Optimal insulation for ice rink floors. *Energy and Buildings*, 108, p. 358-364.
- Myrseth, I., & Omre, H. (2001). The ensemble kalman filter and related filters. In L. Biegler et al. (Eds.), *Large-scale inverse problems and quantification of uncertainty* (p. 217-246). John Wiley & Sons.
- Pfeffer, W. (1986). The divergence theorem. *Transactions of the American Mathematical Society*, 295, p. 665-685.
- Rogstam, J., & Hjert, J. (2010). *Stoppsladd fas 1, energianvändning i svenska isarenor* (Tech. Rep.). Sveriges Energi- & Kylcentrum.
- Silverman, B. (1986). *Density estimation for statistics and data analysis*. Chapman and Hall.
- Somrani, R., Mun, J., & Krarti, M. (2008). Heat transfer beneath ice-rink floors. *Building and Environment*, 43, p. 1687-1698.

Widder, D. (1976). *The heat equation*. Elsevier Science.

Zieniuk, E., Sawicki, D., & Boltuc, A. (2014). Parametric integral equations systems in 2d transient heat conduction analysis. *International Journal of Heat and Mass Transfer*, 78, p. 571-587.